

This is an Open Access document downloaded from ORCA, Cardiff University's institutional repository: <https://orca.cardiff.ac.uk/id/eprint/121048/>

This is the author's version of a work that was submitted to / accepted for publication.

Citation for final published version:

Togni, Riccardo, Cimarelli, Andrea and De Angelis, Elisabetta 2019. Resolved and subgrid dynamics of Rayleigh-Bénard convection. *Journal of Fluid Mechanics* 867 , pp. 906-933. 10.1017/jfm.2019.119

Publishers page: <https://doi.org/10.1017/jfm.2019.119>

Please note:

Changes made as a result of publishing processes such as copy-editing, formatting and page numbers may not be reflected in this version. For the definitive version of this publication, please refer to the published source. You are advised to consult the publisher's version if you wish to cite this paper.

This version is being made available in accordance with publisher policies. See <http://orca.cf.ac.uk/policies.html> for usage policies. Copyright and moral rights for publications made available in ORCA are retained by the copyright holders.



# Resolved and subgrid dynamics of Rayleigh-Bénard convection

Riccardo Togni<sup>1</sup>, Andrea Cimarelli<sup>2</sup> and Elisabetta De Angelis<sup>1,2†</sup>

<sup>1</sup>DIN, Università di Bologna, Via Fontanelle 40, 47121 Forlì, Italy

<sup>2</sup>School of Engineering, Cardiff University, Queen's Buildings, The Parade, Cardiff CF24 3AA, UK

(Received xx; revised xx; accepted xx)

In this work we present and demonstrate the reliability of a theoretical framework for the study of thermally driven turbulence. It consists of scale-by-scale budget equations for the second-order velocity and temperature structure functions and their limiting cases, represented by the turbulent kinetic energy and temperature variance budgets. This framework represents an extension of the classical Kolmogorov and Yaglom equations to inhomogeneous and anisotropic flows, and allows for a novel assessment of the turbulent processes occurring at different scales and locations in the fluid domain. Two relevant characteristic scales,  $\ell_c^u$  for the velocity field and  $\ell_c^\theta$  for the temperature field are identified. These variables separate the space of scales into a quasi-homogeneous range, characterized by turbulent kinetic energy and temperature variance cascades towards dissipation, and an inhomogeneity-dominated range, where the production and the transport in physical space are important. This theoretical framework is then extended to the context of Large-Eddy Simulation (LES) to quantify the effect of a low-pass filtering operation on both resolved and subgrid dynamics of turbulent Rayleigh-Bénard convection. It consists of single-point and scale-by-scale budget equations for the filtered velocity and temperature fields. To evaluate the effect of the filter length  $\ell_F$  on the resolved and subgrid dynamics, the velocity and temperature fields obtained from a Direct Numerical Simulation (DNS) are split into filtered and residual components using a spectral cutoff filter. It is found that when  $\ell_F$  is smaller than the minimum values of the cross-over scales given by  $\ell_{c,min}^{\theta*} = \ell_{c,min}^\theta Nu/H = 0.8$ , the resolved processes correspond to the exact ones, except for a depletion of viscous and thermal dissipations, and the only role of the subgrid scales is to drain turbulent kinetic energy and temperature variance to dissipate them. On the other hand, the resolved dynamics is much poorer in the near-wall region and the effect of the subgrid scales are more complex for filter lengths of the order of  $\ell_F \approx 3 \ell_{c,min}^\theta$  or larger. This study suggests that classic eddy-viscosity/diffusivity models employed in LES may suffer from some limitations for large filter lengths, and that alternative closures should be considered to account for the inhomogeneous processes at subgrid level. Moreover, the theoretical framework based on the filtered Kolmogorov and Yaglom equations may represent a valuable tool for future assessments of the subgrid-scale models.

**Key words:** Thermally-driven turbulence, Scale-by-scale budget, Resolved and subgrid dynamics.

---

† Email address for correspondence: e.deangelis@unibo.it

## 1. Introduction

Since the beginning of computational fluid dynamics, Large-Eddy Simulation (LES) of thermally driven flows has been the subject of many studies in particular for meteorological applications (Smagorinsky 1963; Lilly 1967; Deardorff 1974). The original motivation was driven by the failure of analytical methods in describing the dynamics of the atmosphere, together with the intrinsic limitations of both experimental measurements and numerical solutions of the full governing equations (Lilly 1962). The computational resources required for a Direct Numerical Simulation (DNS) are still prohibitive nowadays for most of the engineering and geophysical flows. However, the steady increase of computing power over the last decades aroused new interest in the LES technique and great effort has been spent to improve its level of feasibility and accuracy (Piomelli 1999).

The correct treatment of the near-wall region represents one of the main challenges in LES because production and transport mechanisms induced by spatial inhomogeneity involve even smaller scales as the boundaries are approached (Porté-Agel *et al.* 2001); hence, the local integral scale of the flow steeply decreases from the bulk to the wall and such a drop can be of several orders of magnitude in systems of practical interest (Piomelli & Balaras 2002). The result is that the computational cost required by a wall-resolved LES, in terms of CPU time and memory, cannot be afforded in case of high Reynolds number flows. To overcome this limitation, a significant reduction of the near-wall resolution is demanded. In this context, it is fundamental to understand which turbulent mechanisms are going to be captured and which are going to be filtered out by an LES. This is important for two distinct but interrelated reasons. In the first place, a clear overview of the resolved dynamics allows for the identification of a minimum resolution requirement, namely the smallest scale of the flow that we aim to solve numerically in order to capture the structures that are more energetic and less universal (Bryan *et al.* 2003). Secondly, the analysis of the subgrid dynamics represents an ideal premise for the formulation of a physically-based subgrid-scale (SGS) model capable to reproduce, as best as possible, the effects of the unresolved scales (Mason 1989).

Following this line of research, the main goal of the present paper is to shed light on the resolved and subgrid dynamics of thermally-driven turbulence via the analysis of a filtered DNS data set. This methodology, called *a priori* in LES studies, can serve as an efficient tool for checking to what extent the resolved physics reproduces the real one and how the SGS model copes with the interplay between resolved and subgrid scales. Due to the inherent complexity of natural and technological flows, we focus our investigation to a canonical system, the Rayleigh-Bénard convection (RBC), commonly defined as a fluid layer confined between two infinite horizontal walls, heated from below and cooled from above (Siggia 1994; Chillà & Schumacher 2012). The RBC is simple enough to be treated by theoretical, numerical and experimental studies, although it preserves the essential features of thermally-driven flows, namely the balance between buoyancy force and viscous/diffusive damping (Ahlers *et al.* 2012; Gayen *et al.* 2013). Some studies have been devoted to the assessment of SGS models for RBC (Cabot 1993; Kimmel & Domaradzki 2000; Sergent *et al.* 2006; Dabbagh *et al.* 2016; Dabbagh *et al.* 2017); however, literature lacks a detailed *a priori* analysis of this system, unlike other paradigmatic flows such as the round jet (Liu *et al.* 1994), the transitional (Piomelli *et al.* 1991) and the stationary channel flows (Härtel *et al.* 1994).

The identification of the local integral scales in RBC is presented in the first part of the work. For this purpose, a DNS data set at Rayleigh number ( $Ra$ )  $1.0 \times 10^7$  and Prandtl number ( $Pr$ ) 0.7 is analyzed with the Kolmogorov and Yaglom equations (Kolmogorov 1941*a*; Yaglom 1949) extended to an inhomogeneous and anisotropic flow

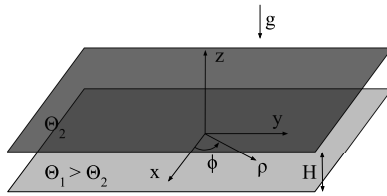


FIGURE 1. Sketch of the Rayleigh-Bénard convection setup.

(Hill 2002; Marati *et al.* 2004; Burattini *et al.* 2005; Valente & Vassilicos 2015). These are the evolution equations for the second-order velocity and temperature structure functions, which can be exactly derived from the governing equations and allow for a neat description of the turbulent processes occurring at different scales and locations in physical space. Two characteristic scales are identified using these budgets, one for the velocity field,  $\ell_c^u$ , and one for the temperature field,  $\ell_c^\theta$ , which depend on the wall-distance and separate the large inhomogeneous scales from the small dissipative ones.

In the LES framework, the relative position of the filter length,  $\ell_F$ , with respect to  $\ell_c^u$  and  $\ell_c^\theta$  determines up to what extent the flow dynamics is going to be captured and what should be reproduced by the SGS model. In particular, for filter lengths smaller than the identified crossover scales, the most inhomogeneous and energetic features of the flow are arguably captured and the purely-dissipative role of the subgrid scales can be reproduced by means of simple and rather universal closures. In the second part of this work, the effect of the filter length on the resolved and subgrid dynamics is rigorously assessed. For this purpose, the velocity and the scalar fields obtained from a DNS are split into resolved and subgrid components using a spectral cutoff filter and analyzed by means of filtered single-point and two-point budgets. While the filtered Kolmogorov equation has been already employed by Cimarelli & De Angelis (2011), the filtered Yaglom equation is presented and discussed here for the first time.

The paper is organized as follows. The theoretical framework consisting of single-point and scale-by-scale budgets is presented in section 2. The fully-resolved dynamics of RBC is then discussed in section 3, followed by the analysis of the filtered data set in section 4. A summary of the main findings and some concluding remarks are made in section 5.

## 2. The Kolmogorov and Yaglom equations

In the framework of homogeneous and isotropic turbulence transporting a passive temperature, the Kolmogorov-Obukhov-Corrsin theory (K41-OC) states that, at sufficiently high Reynolds numbers, a range of scales exists where turbulent kinetic energy and temperature variance are only transferred from large to small scales (Kolmogorov 1941*b*; Obukhov 1968; Corrsin 1951). This exact and non trivial result can be derived from the equations for the second-order velocity and temperature structure functions  $\langle \delta u^2 \rangle = \langle \delta u_i \delta u_i \rangle$  and  $\langle \delta \theta^2 \rangle = \langle \delta \theta \delta \theta \rangle$ . The angular brackets  $\langle \cdot \rangle$  denote the spatial average along the homogeneous directions and the ensemble average over different configurations,  $\delta u_i = u_i(x_j + r_j/2) - u_i(x_j - r_j/2)$  and  $\delta \theta = \theta(x_j + r_j/2) - \theta(x_j - r_j/2)$  are the fluctuating velocity and temperature increments between the points  $x_j + r_j/2$  and  $x_j - r_j/2$ , and the indexes  $i, j = 1, 2, 3$  denote the Cartesian components.

Following the heuristic approach proposed by Davidson *et al.* (2004), the second-order structure functions  $\langle \delta u^2 \rangle$  and  $\langle \delta \theta^2 \rangle$  can be interpreted as the turbulent kinetic energy and the temperature variance, respectively, contained by the eddies of length scale smaller than  $r = \sqrt{r_i r_i}$ . Indeed, turbulent scales less than  $r$  can actively modulate the signal at

$x_j + r_j/2$  or  $x_j - r_j/2$  but not at both locations simultaneously; thus, they contribute significantly to the structure function. On the other hand, eddies of size much larger than  $r$  tend to induce similar signals at both points with consequent little contribution to the fluctuating increment. In summary, the structure function can be considered along the same line as a high-pass filter, capable to retain the fluctuations at scales smaller than the filter length  $r$  and to damp the information from eddies of size larger than  $r$ . Hence, together with the turbulent spectrum, it can be used to study the multi-scale features of turbulence, see e.g. Dupuy *et al.* (2018). In view of this, throughout this paper we will refer to  $\langle \delta u^2 \rangle$  and  $\langle \delta \theta^2 \rangle$  also as *scale energy* and *scale variance* respectively, adopting the nomenclature introduced by Danaila *et al.* (2001) and employed later by Marati *et al.* (2004); Cimarelli & De Angelis (2011); Cimarelli *et al.* (2013); Togni *et al.* (2015).

In general, the second-order structure function depends both on the separation vector  $r_j$  and on the spatial location of the mid-point  $x_j$ . However, in case of homogeneous turbulence the dependence of the scale energy and the scale variance on the mid-point  $x_j$  drops and, starting from the governing equations, it is possible to derive the following exact equations for  $\langle \delta u^2 \rangle$  and  $\langle \delta \theta^2 \rangle$ ,

$$-\frac{\partial \langle \delta u^2 \delta u_i \rangle}{\partial r_i} + 2 \langle \delta f_i^u \delta u_i \rangle + 2\nu \frac{\partial^2 \langle \delta u^2 \rangle}{\partial r_j \partial r_j} - 4 \langle \epsilon \rangle = 0, \quad (2.1)$$

$$-\frac{\partial \langle \delta \theta^2 \delta u_i \rangle}{\partial r_i} + 2 \langle \delta f_i^\theta \delta u_i \rangle + 2\kappa \frac{\partial^2 \langle \delta \theta^2 \rangle}{\partial r_j \partial r_j} - 2 \langle \chi \rangle = 0, \quad (2.2)$$

where  $\nu$  is the kinematic viscosity,  $\kappa$  is the thermal diffusivity,  $\epsilon = 2\nu (S_{ij} S_{ij})$  is the dissipation of turbulent kinetic energy,  $S_{ij} = 0.5 (\partial u_i / \partial x_j + \partial u_j / \partial x_i)$  is the fluctuating strain-rate tensor,  $\chi = 2\kappa (\partial \theta / \partial x_i) (\partial \theta / \partial x_i)$  is the dissipation of temperature variance,  $2 \langle \delta f_i^u \delta u_i \rangle$  and  $2 \langle \delta f_i^\theta \delta u_i \rangle$  are the homogeneous source terms due to the external forcing  $f_i^u$  and  $f_i^\theta$  active at large scales. The first term in (2.1) and (2.2) denotes the rate at which scales smaller than  $r$  receive (release) turbulent kinetic energy and temperature variance from (to) larger ones via inertial mechanisms, whereas the third term in (2.1) and (2.2) is indicative of the amount of turbulent kinetic energy and temperature variance diffused in the space of scales. In case of high intensity turbulent flows, an inertial range is supposed to develop for  $\eta_k, \eta_b \ll r \ll \ell_0$ , where  $\eta_k$ ,  $\eta_b$  and  $\ell_0$  are the Kolmogorov, the Batchelor and the integral scales, respectively. Both production and viscous diffusion effects are negligible within this range, thus (2.1) and (2.2) reduce to

$$\frac{\partial \langle \delta u^2 \delta u_i \rangle}{\partial r_i} = -4 \langle \epsilon \rangle, \quad (2.3)$$

$$\frac{\partial \langle \delta \theta^2 \delta u_i \rangle}{\partial r_i} = -2 \langle \chi \rangle, \quad (2.4)$$

stating that the amount of turbulent kinetic energy and temperature variance transferred per unit time to scales less than  $r$  is equal to the average dissipation rates. It should be pointed out that (2.3) and (2.4) further simplify to the familiar four-fifth and four-third laws respectively, if turbulence is assumed to be also isotropic.

The fundamental aspect of actual turbulent flows is the presence of a cycle along which fluctuations are generated, transported among different scales and space locations, and finally dissipated. Inhomogeneity modifies the scale-by-scale budgets (2.1) and (2.2) by introducing an autonomous production, a transport in physical space and by spatially modulating the balances. Fully-developed turbulence in laterally-unbounded RBC is statistically inhomogeneous in the wall-normal direction but homogeneous and isotropic

in the wall-parallel planes. We exploit these symmetries, and in particular the isotropy in the wall-parallel planes, by considering a cylindrical coordinate system  $(\rho, \phi, z)$  rather than a Cartesian one  $(x, y, z)$ ; see the sketch in figure 1. The wall-parallel coordinates are  $x = x_1$  and  $y = x_2$  while the wall-normal coordinate,  $z = x_3$ , is zero at the lower wall. The cylindrical coordinates are defined such as  $\rho = \sqrt{x^2 + y^2}$  and  $\phi = \arctan(y/x)$ . The scale-by-scale budgets for the RBC can be derived starting from the continuity, momentum and energy equations under the Boussinesq approximation (Hill 2002) and, for a cylindrical coordinate system, result into

$$\begin{aligned} & -\frac{\partial \langle w^\dagger \delta u^2 \rangle}{\partial z} - 2 \frac{\partial \langle \delta p \delta w \rangle}{\partial z} + \frac{\nu}{2} \frac{\partial^2 \langle \delta u^2 \rangle}{\partial z^2} - \frac{1}{r_\rho} \frac{\partial}{\partial r_\rho} (r_\rho \langle \delta u^2 \delta u_\rho \rangle) \\ & - \frac{\partial \langle \delta u^2 \delta w \rangle}{\partial r_z} + 2\alpha g \langle \delta \theta \delta w \rangle + \frac{2\nu}{r_\rho} \frac{\partial}{\partial r_\rho} \left( r_\rho \frac{\partial \langle \delta u^2 \rangle}{\partial r_\rho} \right) + 2\nu \frac{\partial^2 \langle \delta u^2 \rangle}{\partial r_z^2} - 4 \langle \tilde{\epsilon}^\dagger \rangle = 0 \end{aligned} \quad (2.5)$$

and

$$\begin{aligned} & -\frac{\partial \langle w^\dagger \delta \theta^2 \rangle}{\partial z} + \frac{\kappa}{2} \frac{\partial^2 \langle \delta \theta^2 \rangle}{\partial z^2} - \frac{1}{r_\rho} \frac{\partial}{\partial r_\rho} (r_\rho \langle \delta \theta^2 \delta u_\rho \rangle) - \frac{\partial \langle \delta \theta^2 \delta w \rangle}{\partial r_z} \\ & - 2 \langle w^\dagger \delta \theta \rangle \frac{\partial \delta \Theta}{\partial z} - 2 \langle \delta w \delta \theta \rangle \left( \frac{d\Theta}{dz} \right)^\dagger + \frac{2\kappa}{r_\rho} \frac{\partial}{\partial r_\rho} \left( r_\rho \frac{\partial \langle \delta \theta^2 \rangle}{\partial r_\rho} \right) + 2\kappa \frac{\partial^2 \langle \delta \theta^2 \rangle}{\partial r_z^2} \\ & - 2 \langle \chi^\dagger \rangle = 0, \end{aligned} \quad (2.6)$$

where  $g$  is the gravity acceleration,  $\alpha$  is the thermal expansion coefficient and  $\tilde{\epsilon} = \nu (\partial u_i / \partial x_j) (\partial u_i / \partial x_j)$  is the pseudo-dissipation of turbulent kinetic energy. The dagger  $^\dagger$  denotes the mid-point average,  $\beta^\dagger = (\beta(x_j - r_j/2) + \beta(x_j + r_j/2))/2$  for the generic quantity  $\beta$ . The radial, the circumferential and the vertical components of the separation vector are  $r_\rho$ ,  $r_\phi$  and  $r_z$ , whereas the same components of the velocity structure function are  $\delta u_\rho$ ,  $\delta u_\phi$  and  $\delta w$ . Let us notice that all the  $r_\phi$ -derivative terms arising from the formulation in cylindrical coordinates are zero for the statistical isotropy while, for the statistical homogeneity, also the  $\phi$ - and  $\rho$ -derivatives are null.

An additional class of terms, namely the ones with the  $z$ -derivative, appear in the inhomogeneous case, denoting the amount of scale energy and scale variance received (released) from (to) other wall-distances. Moreover,  $2\alpha g \langle \delta \theta \delta w \rangle$  and  $-2 \langle w^\dagger \delta \theta \rangle (\partial \delta \Theta / \partial z) - 2 \langle \delta w \delta \theta \rangle (d\Theta / dz)^\dagger$  are the inhomogeneous production terms, where  $\Theta$  is the mean temperature. At sufficiently high Reynolds numbers, an inertial range of scales is assumed to exist in which turbulence is locally homogeneous and isotropic, viscous effects are negligible and temperature acts as a passive scalar (Lohse & Xia 2010). In this case, it is easy to demonstrate that (2.5) and (2.6) simplify to (2.3) and (2.4) and, with further manipulations, to the four-fifth and four-third laws respectively.

Equations (2.5) and (2.6), written in the complete three-dimensional  $(r_\rho, r_z, z)$ -space, are the Kolmogorov and Yaglom equations for the RBC. The Kolmogorov equation for an axisymmetric flow has already been proposed by Danaila *et al.* (2012) while the Yaglom equation has been extended before only to homogeneous anisotropic turbulence (Gauding *et al.* 2014). For the sake of simplicity, we restrict the following analysis to the reduced  $(r_\rho, z)$ -space, where  $r_z = 0$  (Cimarelli *et al.* 2016). The reduced scale-by-scale budgets are non-dimensionalized using  $H$ ,  $\Delta\Theta = \Theta_1 - \Theta_2$  and  $U_f = \sqrt{g\alpha\Delta\Theta H}$  as characteristic length, temperature and velocity scales, where  $H$  is the height of the fluid layer,  $\Theta_1$  and  $\Theta_2$  are the temperature of the lower and upper walls respectively,  $U_f$  is the free-

fall velocity. The resulting equations, hereafter referred to as *reduced* Kolmogorov and Yaglom equations, can be written in a compact form, i.e.

$$T_c^u + I_r^u + \Pi^u + E_e^u = 0, \quad (2.7)$$

$$T_c^\theta + I_r^\theta + \Pi^\theta + E_e^\theta = 0, \quad (2.8)$$

where  $T_c^u = I_c^u + P + D_c^u$  and  $T_c^\theta = I_c^\theta + D_c^\theta$  represent the sum of the transport terms in physical space and, hence, will be hereafter called the *overall transports*. On the other hand,  $E_e^u = D_r^u + E^u$  and  $E_e^\theta = D_r^\theta + E^\theta$  represent the overall effect of viscosity on transporting scale energy and scale variance to the smallest scales of the flow by  $D_r^u$  and  $D_r^\theta$ , where are finally dissipated by  $E^u$  and  $E^\theta$ . Accordingly,  $E_e^u$  and  $E_e^\theta$  will be hereafter called *effective dissipations*. The different contributions to the overall transports and to the effective dissipations are, in order,

$$I_c^u = -\frac{\partial \langle w^\dagger \delta u^2 \rangle}{\partial z}, \quad P = -2 \frac{\partial \langle \delta p \delta w \rangle}{\partial z}, \quad D_c^u = \frac{1}{2} \sqrt{\frac{Pr}{Ra}} \frac{\partial^2 \langle \delta u^2 \rangle}{\partial z^2},$$

$$I_c^\theta = -\frac{\partial \langle w^\dagger \delta \theta^2 \rangle}{\partial z}, \quad D_c^\theta = \frac{1}{2\sqrt{PrRa}} \frac{\partial^2 \langle \delta \theta^2 \rangle}{\partial z^2},$$

and

$$D_r^u = 2\sqrt{\frac{Pr}{Ra}} \frac{1}{r_\rho} \frac{\partial}{\partial r_\rho} \left( r_\rho \frac{\partial \langle \delta u^2 \rangle}{\partial r_\rho} \right) + 2\sqrt{\frac{Pr}{Ra}} \frac{\partial^2 \langle \delta u^2 \rangle}{\partial r_z^2} \Big|_{r_z=0}, \quad E^u = -4 \langle \tilde{\epsilon} \rangle,$$

$$D_r^\theta = \frac{2}{\sqrt{PrRa}} \frac{1}{r_\rho} \frac{\partial}{\partial r_\rho} \left( r_\rho \frac{\partial \langle \delta \theta^2 \rangle}{\partial r_\rho} \right) + \frac{2}{\sqrt{PrRa}} \frac{\partial^2 \langle \delta \theta^2 \rangle}{\partial r_z^2} \Big|_{r_z=0}, \quad E^\theta = -2 \langle \chi \rangle,$$

while the transports in the space of scales and the production terms are

$$I_r^u = -\frac{1}{r_\rho} \frac{\partial}{\partial r_\rho} (r_\rho \langle \delta u^2 \delta u_\rho \rangle) - \frac{\partial \langle \delta u^2 \delta w \rangle}{\partial r_z} \Big|_{r_z=0}, \quad \Pi^u = 2 \langle \delta \theta \delta w \rangle,$$

$$I_r^\theta = -\frac{1}{r_\rho} \frac{\partial}{\partial r_\rho} (r_\rho \langle \delta \theta^2 \delta u_\rho \rangle) - \frac{\partial \langle \delta \theta^2 \delta w \rangle}{\partial r_z} \Big|_{r_z=0}, \quad \Pi^\theta = -2 \langle \delta w \delta \theta \rangle \frac{d\Theta}{dz}.$$

It must be pointed out that the contribution of the term  $-2 \langle w^\dagger \delta \theta \rangle (\partial \delta \Theta / \partial z)$  to the production of scale variance vanishes, since  $\delta \Theta = 0$  for  $r_z = 0$ . Finally, the non-dimensional groups appearing are the Rayleigh number,  $Ra = g\alpha\Delta\Theta H^3/\nu\kappa$ , and the Prandtl number,  $Pr = \nu/\kappa$ .

Let us extend the Kolmogorov and Yaglom equations to filtered velocity and temperature fields. Starting from the filtered continuity, momentum and energy equations under the Boussinesq approximation and by following the same procedure used to derive (2.5) and (2.6) (Hill 2002), it is possible to obtain the budgets of resolved scale energy

$\langle \delta \bar{u}^2 \rangle = \langle \delta \bar{u}_i \delta \bar{u}_i \rangle$  and resolved scale variance  $\langle \delta \bar{\theta}^2 \rangle = \langle \delta \bar{\theta} \delta \bar{\theta} \rangle$ ,

$$\begin{aligned} & -\frac{\partial \langle \bar{w}^\dagger \delta \bar{u}^2 \rangle}{\partial z} - 2 \frac{\partial \langle \delta \bar{p} \delta \bar{w} \rangle}{\partial z} + \frac{\nu}{2} \frac{\partial^2 \langle \delta \bar{u}^2 \rangle}{\partial z^2} - \frac{1}{r_\rho} \frac{\partial}{\partial r_\rho} (r_\rho \langle \delta \bar{u}^2 \delta \bar{u}_\rho \rangle) \\ & - \frac{\partial \langle \delta \bar{u}^2 \delta \bar{w} \rangle}{\partial r_z} + 2\alpha g \langle \delta \bar{\theta} \delta \bar{w} \rangle + \frac{2\nu}{r_\rho} \frac{\partial}{\partial r_\rho} \left( r_\rho \frac{\partial \langle \delta \bar{u}^2 \rangle}{\partial r_\rho} \right) + 2\nu \frac{\partial^2 \langle \delta \bar{u}^2 \rangle}{\partial r_z^2} - 4 \langle \bar{\epsilon}^\dagger \rangle \quad (2.9) \\ & - \frac{\partial \langle \delta \tau_{i3} \delta \bar{u}_i \rangle}{\partial z} - \frac{4}{r_\rho} \frac{\partial}{\partial r_\rho} \left( r_\rho \langle \tau_{ij}^\dagger \delta \bar{u}_i \hat{\rho}_j \rangle \right) - 4 \frac{\partial \langle \tau_{i3}^\dagger \delta \bar{u}_i \rangle}{\partial r_z} \Big|_{r_z=0} - 4 \langle \epsilon_{sgs} \rangle = 0 \end{aligned}$$

and

$$\begin{aligned} & -\frac{\partial \langle \bar{w}^\dagger \delta \bar{\theta}^2 \rangle}{\partial z} + \frac{\kappa}{2} \frac{\partial^2 \langle \delta \bar{\theta}^2 \rangle}{\partial z^2} - \frac{1}{r_\rho} \frac{\partial}{\partial r_\rho} (r_\rho \langle \delta \bar{\theta}^2 \delta \bar{u}_\rho \rangle) - \frac{\partial \langle \delta \bar{\theta}^2 \delta \bar{w} \rangle}{\partial r_z} \\ & - 2 \langle \bar{w}^\dagger \delta \bar{\theta} \rangle \frac{\partial \delta \bar{\theta}}{\partial z} - 2 \langle \delta \bar{w} \delta \bar{\theta} \rangle \left( \frac{d\bar{\theta}}{dz} \right)^\dagger + \frac{2\kappa}{r_\rho} \frac{\partial}{\partial r_\rho} \left( r_\rho \frac{\partial \langle \delta \bar{\theta}^2 \rangle}{\partial r_\rho} \right) + 2\kappa \frac{\partial^2 \langle \delta \bar{\theta}^2 \rangle}{\partial r_z^2} \quad (2.10) \\ & - 2 \langle \bar{\chi}^\dagger \rangle - \frac{\partial \langle \delta q_z \delta \bar{\theta} \rangle}{\partial z} - \frac{4}{r_\rho} \frac{\partial}{\partial r_\rho} (r_\rho \langle q_\rho^\dagger \delta \bar{\theta} \rangle) - 4 \frac{\partial \langle q_z^\dagger \delta \bar{\theta} \rangle}{\partial r_z} \Big|_{r_z=0} - 2 \langle \chi_{sgs} \rangle = 0. \end{aligned}$$

Equations (2.9) and (2.10) share several type of terms with the corresponding unfiltered equations (2.5) and (2.6) which can be better highlighted by considering the *filtered reduced* Kolmogorov and Yaglom equations

$$\bar{T}_c^u + \bar{I}_r^u + \bar{H}^u + \bar{E}_e^u + T_{c,sgs}^u + T_{r,sgs}^u + E_{sgs}^u = 0, \quad (2.11)$$

$$\bar{T}_c^\theta + \bar{I}_r^\theta + \bar{H}^\theta + \bar{E}_e^\theta + T_{c,sgs}^\theta + T_{r,sgs}^\theta + E_{sgs}^\theta = 0, \quad (2.12)$$

where it is possible to recognize that the first four terms in (2.11) and (2.12) are the same terms composing the unfiltered reduced budgets (2.7) and (2.8) with the difference that are constituted by the filtered velocity, temperature and pressure fields. Indeed, the completely new terms in the filtered budgets are entirely due to subgrid scale effects, i.e.

$$\begin{aligned} T_{c,sgs}^u &= -\frac{\partial \langle \delta \tau_{i3} \delta \bar{u}_i \rangle}{\partial z}, \quad T_{r,sgs}^u = -\frac{4}{r_\rho} \frac{\partial}{\partial r_\rho} \left( r_\rho \langle \tau_{ij}^\dagger \delta \bar{u}_i \hat{\rho}_j \rangle \right) - 4 \frac{\partial \langle \tau_{i3}^\dagger \delta \bar{u}_i \rangle}{\partial r_z} \Big|_{r_z=0}, \\ E_{sgs}^u &= -4 \langle \epsilon_{sgs} \rangle, \\ T_{c,sgs}^\theta &= -\frac{\partial \langle \delta q_z \delta \bar{\theta} \rangle}{\partial z}, \quad T_{r,sgs}^\theta = -\frac{4}{r_\rho} \frac{\partial}{\partial r_\rho} (r_\rho \langle q_\rho^\dagger \delta \bar{\theta} \rangle) - 4 \frac{\partial \langle q_z^\dagger \delta \bar{\theta} \rangle}{\partial r_z} \Big|_{r_z=0}, \\ E_{sgs}^\theta &= -2 \langle \chi_{sgs} \rangle, \end{aligned}$$

and represent the transport in physical space, the transport in the space of scales and the dissipation of resolved scale energy and resolved scale variance due to the fluctuating SGS stress tensor,  $\tau_{ij} = \bar{u}_i \bar{u}_j - \bar{u}_i \bar{u}_j$ , and the fluctuating SGS heat flux,  $q_i = \bar{u}_i \bar{\theta} - \bar{u}_i \bar{\theta}$ . Here,  $q_\rho$  and  $q_z$  are the radial and vertical components of the SGS heat flux,  $\hat{\rho}_j$  is the radial unit vector,  $\bar{\epsilon} = \sqrt{Pr/Ra} (\partial \bar{u}_i / \partial x_j) (\partial \bar{u}_i / \partial x_j)$  is the pseudo-dissipation of resolved turbulent kinetic energy and  $\bar{\chi} = 2 (PrRa)^{-1/2} (\partial \bar{\theta} / \partial x_i) (\partial \bar{\theta} / \partial x_i)$  is the dissipation of resolved temperature variance. The subgrid dissipations are  $\epsilon_{sgs} = -\tau_{ij} \bar{S}_{ij}$  and  $\chi_{sgs} = -2q_i \bar{Q}_i$ ,



where  $\bar{S}_{ij} = 0.5 (\partial \bar{u}_i / \partial x_j + \partial \bar{u}_j / \partial x_i)$  is the resolved fluctuating strain-rate tensor and  $\bar{Q}_i = \partial \bar{\theta} / \partial x_i$  is the gradient of the resolved fluctuating temperature.

Let us point out that the filtered reduced Kolmogorov equation (2.11) has been already employed for the *a priori* (Cimarelli & De Angelis 2012) and the *a posteriori* (Cimarelli & De Angelis 2014) test of some SGS models for the turbulent channel flow, proving to be a precious framework for the assessment of the dynamics induced by  $\tau_{ij}$ . The filtered reduced Yaglom equation (2.12), on the other hand, is presented here for the first time.

Equations (2.7), (2.8) and (2.11), (2.12) manifest a well-defined asymptotic behaviour as larger separations are approached. For  $r_\rho \gg \ell$ , where  $\ell$  is the relevant correlation length, quantities evaluated at  $(\rho + r_\rho/2, \phi, z)$  and  $(\rho - r_\rho/2, \phi, z)$  become uncorrelated and (2.7), (2.8) reduce, within a factor of four and two respectively, to the budgets of turbulent kinetic energy  $\langle k \rangle = 0.5 \langle u_i u_i \rangle$  and temperature variance  $\langle \theta^2 \rangle$ ,

$$4(t_c^u + \pi^u - \langle \bar{\epsilon} \rangle) = 0, \quad (2.13)$$

$$2(t_c^\theta + \pi^\theta - \langle \bar{\chi} \rangle) = 0, \quad (2.14)$$

where

$$t_c^u = -\frac{d\langle kw \rangle}{dz} - \frac{d\langle wp \rangle}{dz} + \sqrt{\frac{Pr}{Ra}} \frac{d^2 \langle k \rangle}{dz^2}, \quad \pi^u = \langle w\theta \rangle,$$

$$t_c^\theta = -\frac{d\langle \theta^2 w \rangle}{dz} + \frac{1}{\sqrt{PrRa}} \frac{d^2 \langle \theta^2 \rangle}{dz^2}, \quad \pi^\theta = -2\langle w\theta \rangle \frac{d\Theta}{dz},$$

are the overall transports and the productions of  $\langle k \rangle$  and  $\langle \theta^2 \rangle$ . Analogously, the filtered reduced Kolmogorov and Yaglom equations converge respectively to four-times the budget of resolved turbulent kinetic energy  $\bar{k} = 0.5(\bar{u}_i \bar{u}_i)$  and two-times the budget of resolved temperature variance  $\langle \bar{\theta}^2 \rangle$ ,

$$4(\bar{t}_c^u + \bar{\pi}^u - \langle \bar{\epsilon} \rangle) + t_{c,sgs}^u - \langle \epsilon_{sgs} \rangle = 0, \quad (2.15)$$

$$2(\bar{t}_c^\theta + \bar{\pi}^\theta - \langle \bar{\chi} \rangle) + t_{c,sgs}^\theta - \langle \chi_{sgs} \rangle = 0, \quad (2.16)$$

where the terms under the overbar and the corresponding ones without it are identical except that they consider filtered quantities. Finally, the SGS transports of  $\langle \bar{k} \rangle$  and  $\langle \bar{\theta}^2 \rangle$  are

$$t_{c,sgs}^u = -\frac{d\langle \tau_{i3} \bar{u}_i \rangle}{dz} \quad \text{and} \quad t_{c,sgs}^\theta = -2 \frac{d\langle q_z \bar{\theta} \rangle}{dz}.$$

It is well known that the thermal boundary layer thickness represents a characteristic length scale in turbulent RBC. As a result of that, in what follows, we analyze all the budgets presented up to now as a function of spatial variables that are nondimensionalized with respect to  $H/Nu$  instead of  $H$ , where  $Nu$  is the Nusselt number, and we denote them with the superscript  $*$ . The choice of the length scale  $H/Nu$ , which is twice the commonly defined thermal boundary layer thickness, allows for a more appropriate comparison of the results when different Rayleigh numbers are considered. In particular, as shown in Togni *et al.* (2015), by normalizing the independent variables with  $H/Nu$ , the shape of temperature statistics becomes  $Ra$ -invariant, whereas the velocity statistics exhibit a rather small drift in the profile shape.

### 3. Study of the unfiltered data set

The reduced Kolmogorov and Yaglom equations, (2.7) and (2.8) respectively, represent two useful tools for investigating the self-sustained mechanisms of convective turbulence

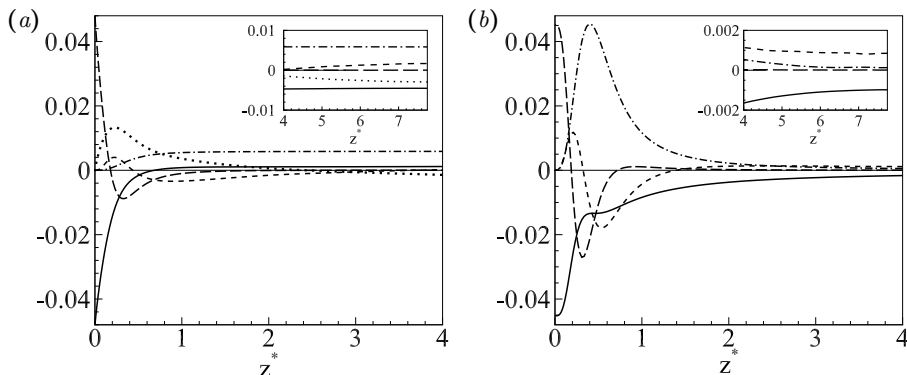


FIGURE 2. (a) Terms of the turbulent kinetic energy budget (2.13) as a function of  $z^*$ : inertial transport (dashed line), pressure transport (dotted line), viscous transport (long dashed line), production (dot-dashed line) and dissipation (solid line). (b) Terms of the temperature variance budget (2.14) as a function of  $z^*$ : inertial transport (dashed line), viscous transport (long dashed line), production (dot-dashed line) and dissipation (solid line).

at different scales and locations in physical space. The essential features of the multi-scale analysis are reported in this section, drawing the attention to their relevance in the LES framework. A thorough description of the budgets is beyond the purpose of this work; hence, we would like to address the reader to Togni *et al.* (2015) for further details. See also Antonia & Orlandi (2003) for additional information on the temperature structure function scaling at different Schmidt numbers.

Each term of (2.7) and (2.8) is computed using a DNS data set of turbulent RBC at  $Ra = 1.0 \times 10^7$  and  $Pr = 0.7$ . The numerical simulation solves the continuity, momentum and energy equations under the Boussinesq approximation using a pseudospectral method that discretizes the space with Chebyshev polynomials in the wall-normal direction and with Fourier modes in the wall-parallel ones. Time integration is performed with a fourth-order Runge-Kutta scheme for the nonlinear terms and a second-order-accurate Crank-Nicolson scheme for the linear ones. The dimensions of the numerical box are  $8 \times 8 \times 1$  along  $x$ ,  $y$ ,  $z$ , where periodic boundary conditions are imposed at the lateral sidewalls and isothermal/no-slip boundary conditions are used on the top and bottom plates. The DNS approach requires a number of fully dealiased modes ( $N_x$ ,  $N_y$ ) and polynomials ( $N_z$ ) to be sufficiently high to resolve all the degrees of freedom of the system. The present simulation is performed with  $N_x \times N_y \times N_z = 540 \times 540 \times 257$  and, as shown in Togni *et al.* (2015) where the details of the present simulation are reported, *a posteriori* tests prove that this resolution is sufficient to capture the smallest scale of the flow. Regarding the temporal advancement, an adaptive time step is set to ensure a Courant-Friedrichs-Lewy number below 2.5. For the sake of statistical convergence, after the initial transient of the flow, the DNS is run for a time period  $T = 250$ , which corresponds to 125 times the large-eddy-turnover time  $2H/U_f = 2$ , and the fields are stored every  $\Delta\tau = 5$  in order to collect samples that are likely uncorrelated. An estimate of the statistical convergence of the data is given by the accuracy with which the Kolmogorov and Yaglom equations are satisfied; see the circles shown in figure 3.

Before presenting the scale-by-scale results, let us report a brief description of the flow dynamics in terms of the single-point budgets of turbulent kinetic energy and temperature variance; see equations (2.13) and (2.14) respectively. According to this analysis, the domain can be split into three fundamental parts: a bulk region for  $0.8 \lesssim z^* < 7.8$  (where  $z^* = Nu/2 = 7.8$  corresponds to the center of the cell), a transitional layer

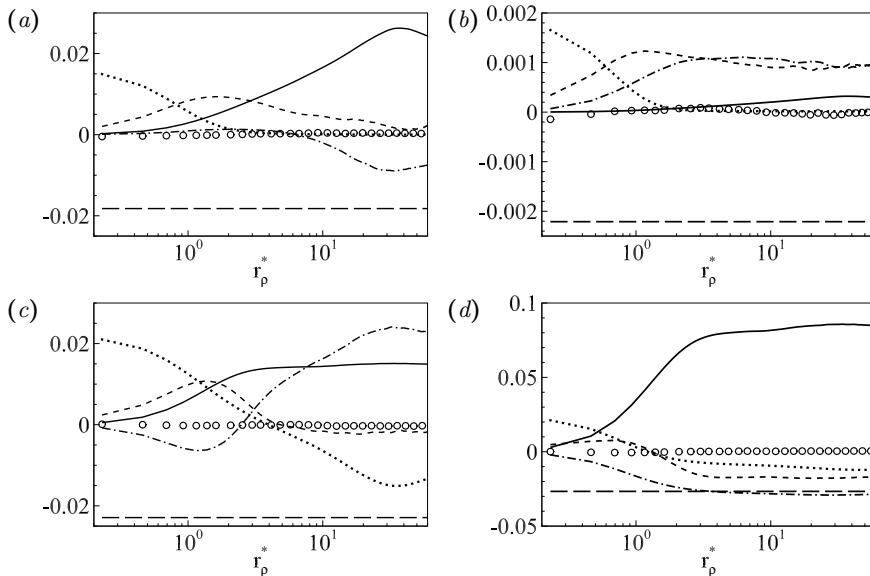


FIGURE 3. (a),(c) Scale-by-scale budgets of  $\langle \delta u^2 \rangle$  and (b),(d) of  $\langle \delta \theta^2 \rangle$  as function of  $r_\rho^*$  inside (a),(b) the bulk region at  $z^* = 6$  and inside (c),(d) the transitional layer at  $z^* = 0.5$ .  $\Pi^u$  and  $\Pi^\theta$  (solid line),  $T_c^u$  and  $T_c^\theta$  (dashed-dot line),  $I_r^u$  and  $I_r^\theta$  (dashed line),  $D_r^u$  and  $D_r^\theta$  (dotted line),  $E^u$  and  $E^\theta$  (long-dashed line),  $T_c^u + I_r^u + D_r^u + \Pi^u + E^u$  and  $T_c^\theta + I_r^\theta + D_r^\theta + \Pi^\theta + E^\theta$  (circles). The maximum separation  $r_\rho^* = 60 \approx 4Nu$  is limited by periodicity along  $x$  and  $y$ .

for  $0.2 \lesssim z^* \lesssim 0.8$  and a viscous layer for  $z^* \lesssim 0.2$ ; see figure 2(a,b). The buoyant production of turbulent kinetic energy overcomes the viscous dissipation inside the bulk region and the resulting excess of energy is mostly transported towards the wall by means of pressure mechanisms. The transitional region, located between the bulk and the viscous layer, is sustained by the inviscid transport coming from the core rather than by the local production; from there, energy diffuses into the viscous layer where it balances the local dissipation rate. Regarding the budget for the temperature variance, the transitional layer is a source region that irradiates thermal fluctuations towards the bulk and towards the viscous layer by means of inertial and viscous mechanisms. The bulk region and the viscous layer are, on the other hand, two sink regions for thermal fluctuations, as they mostly receive and dissipate the temperature variance that is generated inside the transitional layer. See Togni *et al.* (2015) for a detailed discussion of the turbulent kinetic energy and temperature variance budgets.

The mechanisms of production, transport and dissipation of turbulent fluctuations are inherently multi-scale; therefore, they depend not only on the location in physical space but also on the length scale considered. The reduced Kolmogorov and Yaglom equations partially describe this complex phenomenology by addressing the dynamics at separations in the horizontal planes (i.e. for  $r_z^* = 0$ ), and at different wall-distances  $z^*$ . Here, to avoid the complexity that a detailed investigation would imply, we only evaluate the Kolmogorov and Yaglom equations at two relevant distances from the wall,  $z^* = 6$  and  $z^* = 0.5$ , as representative of the typical scale-by-scale behaviours in the bulk region and transitional layer, respectively.

Let us first consider the bulk region. As shown in figure 3(a), the examination of the reduced Kolmogorov equation from large to small  $r_\rho^*$  reveals a range of separations where the production  $\Pi^u$  is important ( $r_\rho^* \gtrsim 3$ ), followed by a range dominated by a positive

inertial transfer,  $I_r^u > 0$  ( $1 \lesssim r_\rho^* \lesssim 3$ ). Inside the inertia-dominated range, scales smaller than those separations receive energy from larger ones via a *direct cascade* rather than produce it by themselves. At even smaller separations ( $r_\rho^* \lesssim 1$ )  $D_r^u$  increases up to  $E^u$ , which means that eddies of size less than  $r_\rho^*$  start to be affected by viscous mechanisms and to dissipate the energy cascading from larger ones.

It is worth noting that both the production  $\Pi^u$  and the overall transport  $T_c^u$  reach a well-defined maximum around  $r_\rho^* = 40$ , meaning that turbulent kinetic energy is essentially produced and transported by eddies smaller than this characteristic length. Such an intriguing behaviour can be further investigated by expanding the production term as follows

$$\Pi^u(r_\rho, z) = \Pi_I^u(z) - \Pi_{II}^u(r_\rho, z),$$

where

$$\Pi_I^u = 4 \langle \theta w \rangle \quad \text{and} \quad \Pi_{II}^u = 4 \langle \theta(\rho + r_\rho/2, \phi, z) w(\rho - r_\rho/2, \phi, z) \rangle$$

are, in order, four-times the production of turbulent kinetic energy and four-times the two-point cross-correlation between vertical velocity and temperature fluctuation. It is evident that, for every wall-distance, the maximum of  $\Pi^u$  occurs at the separation which maximizes  $-\Pi_{II}^u$  or, in other words, at the distance where  $w$  and  $\theta$  are maximally anti-correlated. Hence, the characteristic length  $r_\rho^* = 40$  seems to be strictly connected with the flow topology, as it represents a measure of the average distance between warm fluid moving upwards and cold fluid moving downwards. Evidences of large-scale circulations, namely clusters of ascending warm and descending cold plumes, have been reported also in absence of a lateral confinement and these structures show a lateral size that is around two-times the height of the domain, i.e. comparable with the location of the maximum around  $r_\rho^* = 40$  (Van Reeuwijk *et al.* 2005).

The terms of the reduced Yaglom equation are represented in figure 3(b) for the same location in the bulk. In this case, the production  $\Pi^\theta$  is negligible in comparison with the overall transport  $T_c^\theta$  at every separation; however, a range dominated by the term  $T_c^\theta$  due to the spatial inhomogeneity ( $r_\rho^* \gtrsim 3$ ), followed by a direct cascade ( $0.5 \lesssim r_\rho^* \lesssim 3$ ) and closed by dissipation ( $r_\rho^* \lesssim 0.5$ ) can be identified as in figure 3(a). Here, it is worth noting that the overall transport in physical space does not exhibit an evident peak like in the reduced Kolmogorov equation; thus, a characteristic length of the inhomogeneous processes cannot be equally identified.

A completely different scenario occurs inside the transitional layer. As shown in figure 3(c), the analysis of the reduced Kolmogorov equation at  $z^* = 0.5$ , reveals that a production-dominated range, followed by an inertial direct cascade, is no more recognizable. Indeed, both the production and the transport in physical space are important throughout the entire range of separations, while the viscous dissipation is not restricted only to the small scales but substantially affects also the larger ones, as can be seen from the well-defined peak of  $D_r^u$  at  $r_\rho^* \approx 35$ . For  $r_\rho^* \gtrsim 5$ , the net amount of energy produced and transported at scales less than  $r_\rho^*$  can not be entirely dissipated at this wall-distance, i.e.  $\Pi^u + T_c^u > -E_e^u$ , hence velocity fluctuations start to flow towards larger scales in a *reverse cascade* process,  $I_r^u < 0$ , to be finally dissipated at other locations in physical space (Cimarelli *et al.* 2013).

The analysis of the reduced Yaglom equation, shown in figure 3(d) for  $z^* = 0.5$ , leads to similar conclusions. Both the inhomogeneous production  $\Pi^\theta$  and the overall transport  $T_c^\theta$  are dominant down to very small scales. A reverse cascade,  $I_r^\theta < 0$ , can be identified for separations  $r_\rho^* \gtrsim 1.5$  due to the imbalance between the high production and the weak drain associated to transport and dissipation at scales less than  $r_\rho^*$ .

The complex picture emerging from the scale-by-scale analysis can be rationalized

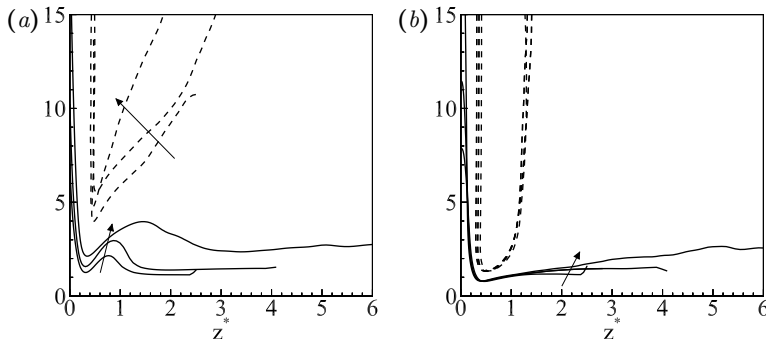


FIGURE 4. (a) Velocity crossover scale  $\ell_c^{u*}$  (solid lines) and boundary scale  $\ell_b^{u*}$  (dashed lines), (b) temperature crossover scale  $\ell_c^{\theta*}$  (solid lines) and boundary scale  $\ell_b^{\theta*}$  (dashed lines) for  $Ra = 1.7 \times 10^5$ ,  $Ra = 1.0 \times 10^6$  and  $Ra = 1.0 \times 10^7$ , where the Rayleigh number increases in the direction of the arrows.

by isolating some fundamental regions inside the reduced  $(r_\rho^*, z^*)$ -space. In light of the observations made in the previous few paragraphs, it is reasonable to split the separations into an inhomogeneity-dominated range at large  $r_\rho^*$  and a quasi-homogeneous range at small  $r_\rho^*$ , where the crossover scales are denoted as  $\ell_c^{u*}$  and  $\ell_c^{\theta*}$ , and satisfy the relations

$$\Pi^u(\ell_c^{u*}, z^*) + T_c^u(\ell_c^{u*}, z^*) = I_r^u(\ell_c^{u*}, z^*) + D_r^u(\ell_c^{u*}, z^*), \quad (3.1)$$

$$\Pi^\theta(\ell_c^{\theta*}, z^*) + T_c^\theta(\ell_c^{\theta*}, z^*) = I_r^\theta(\ell_c^{\theta*}, z^*) + D_r^\theta(\ell_c^{\theta*}, z^*). \quad (3.2)$$

While a direct cascade towards dissipation represents the fundamental mechanism for  $r_\rho^* \lesssim \ell_c^{u*}$  and  $r_\rho^* \lesssim \ell_c^{\theta*}$ , the behaviour due the spatial inhomogeneity can not be neglected for  $r_\rho^* \gtrsim \ell_c^{u*}$  and  $r_\rho^* \gtrsim \ell_c^{\theta*}$ . Inside the inhomogeneous range, the joined action of the production and the overall transport in physical space modulates actively the transfer in the space of scales up to entail a reverse cascade. Hence, the additional scales  $\ell_b^{u*}$  and  $\ell_b^{\theta*}$ , satisfying  $I_r^u(\ell_b^{u*}) = 0$  and  $I_r^\theta(\ell_b^{\theta*}) = 0$ , can be introduced to mark the boundary between the direct cascade and the reverse cascade, completing a concise picture of the flow that accounts only for the most relevant processes.

The velocity and temperature characteristic scales are represented as a function of the wall-distance in figure 4(a,b) for  $Ra = 1.7 \times 10^5$ ,  $Ra = 1.0 \times 10^6$  and  $Ra = 1.0 \times 10^7$ , where the Prandtl number is equal to 0.7. The supplementary data sets at lower  $Ra$  come from two DNS performed with the same numerical domain and boundary conditions as the main DNS at  $Ra = 1.0 \times 10^7$ . As shown in figure 4(a,b), the boundary scales between forward and reverse cascades,  $\ell_b^{u*}$  and  $\ell_b^{\theta*}$ , exceed the corresponding crossover scales between small homogeneous and large inhomogeneous scales,  $\ell_c^{u*}$  and  $\ell_c^{\theta*}$ , at every wall-distance. All the characteristic scales reach a minimum value in the near-wall region around  $z^* \approx 0.2 \div 0.6$ , and then increase inside the viscous/diffusive layer. However, while  $\ell_c^{u*}$  and  $\ell_c^{\theta*}$  are defined along the entire domain,  $\ell_b^{u*}$  and  $\ell_b^{\theta*}$  are defined in a region close to the wall, where the reverse cascades occur.

Interestingly, the characteristic scales of the temperature are shown to be substantially  $Ra$ -independent while those of the velocity increase monotonically with the Rayleigh number. What we observe is due to the fact that the terms of the Yaglom equation do not change their shape with respect to  $r_\rho^*$  and  $z^*$ , hence the crossover and boundary scales are unaltered by  $Ra$ . On the other hand, the Rayleigh number slightly modulates the shape of the Kolmogorov equation terms, thus  $\ell_c^{u*}$  and  $\ell_b^{u*}$  are  $Ra$ -dependent. In view of this, the smallest characteristic scale of the flow is imposed by the temperature

field and it is equal to  $\ell_{c,min}^{\theta*} \approx 0.8$  independently from the Rayleigh number. Moreover, we expect the temperature field to determine the minimum characteristic scale also for higher  $Pr$  due to the augmented separation between diffusive and viscous scales.

In the context of LES, the relative position of the filter length  $\ell_F^*$  with respect to the crossover scales is indicative of what mechanisms can be directly solved and what others should eventually be accounted by an SGS model. If we consider a primary task to capture the large production and energy-containing scales, then the LES should employ filter lengths smaller than  $\ell_{c,min}^{\theta*}$ . Let us point out that such a constraint for the filter width is  $Ra$ -invariant; hence, it can be quantified *a priori* for different Rayleigh numbers and for a fixed Prandtl, as long as an estimation of the Nusselt number is available (Grossmann & Lohse 2000). Accordingly with the definition, for filter lengths smaller than  $\ell_{c,min}^{\theta*}$ , the unresolved mechanism that need to be modeled is essentially the dissipation of turbulent kinetic energy and temperature variance; therefore, classic eddy-viscosity and eddy-diffusivity closures should be capable to provide good results. On the other hand, for filter lengths falling outside the homogeneous range, the physics captured by the LES is expected to be rather poor and the complexity of the phenomena occurring at subgrid level may bring some modelling issues. Regarding the latter point, an increase of the filter length beyond the boundary scales  $\ell_b^{u*}$  and  $\ell_b^{\theta*}$  could generate a net flux taking origin at subgrid level to feed the larger resolved scales via a reverse cascade, as shown by Cimarelli & De Angelis (2011) in the case of a turbulent channel flow. These conditions are a challenge for LES models, which should take into account strong backscatter effects (Cimarelli & De Angelis 2014).

#### 4. Study of the filtered data set

The filtering operation is a crucial stage in LES because it is conditioned by the fundamental and competing tasks of obtaining a reliable and accurate solution on one side, and to limit the computational expense on the other (Pope 2001). The choice of wide filter lengths allows computations to be performed on coarse grids and therefore it requires little computational resources, on the other hand the physics resolved by the LES is quite poor and the solution strongly depends on the choice of the SGS model due to the large extent of the range of subgrid scales.

In order to disentangle the two distinct effects that the filtering operation has on the LES result, namely the degree of resolution of the actual dynamics and the influence of the modelling, a DNS data set can be explicitly filtered to separate the resolved from the subgrid components of the different fields. This *a priori* approach was pursued by many authors in order to compute quantities of interest such as the equations for the filtered turbulent kinetic energy (Härtel *et al.* 1994), the filtered energy spectrum (Domaradzki *et al.* 1994) and the filtered scale energy (Cimarelli & De Angelis 2011).

The mathematical tools that we propose in this study are the filtered single-point budgets, (2.15) and (2.16), and their multi-scale generalization, namely the filtered reduced Kolmogorov (2.11) and Yaglom (2.12) equations. The filtered turbulent kinetic energy and temperature variance equations, to the authors knowledge, have never been completely analyzed in case of RBC, thus section 4.1 has the purpose to present some results that are both novel and preparatory to the filtered multi-scale analysis presented in the following sections, 4.2 and 4.3. The DNS data set at  $Ra = 1.0 \times 10^7$  is split into resolved and subgrid components by applying a sharp cutoff filter in Fourier space in each of the wall-parallel directions,  $x$  and  $y$ , but not in the wall-normal direction  $z$  (Härtel *et al.* 1994; Domaradzki *et al.* 1994). In what follows, the filtered budgets are analyzed for filter lengths  $\ell_F^* = (\pi H)/(\kappa_c Nu)$  ranging from 0.7 to 3.1, where  $\kappa_c$  is the cutoff wavenumber.

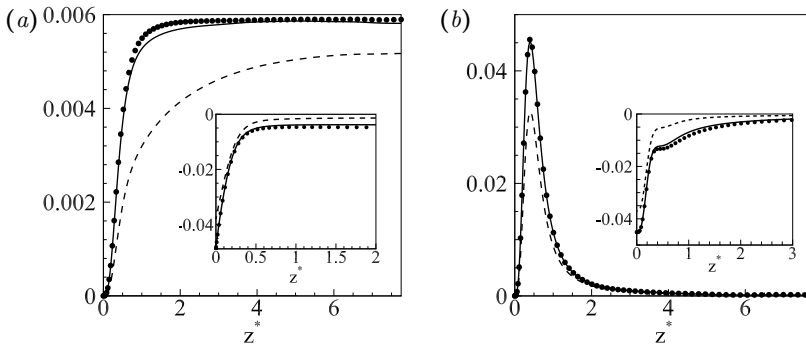


FIGURE 5. Unfiltered and resolved production of (a) turbulent kinetic energy (circles for the unfiltered case, solid line for  $\ell_F^* = 1.0$  and dashed line for  $\ell_F^* = 3.1$ ) and (b) temperature variance (circles for the unfiltered case, solid line for  $\ell_F^* = 0.7$  and dashed line for  $\ell_F^* = 2.1$ ). Insets: unfiltered and resolved dissipation of (a) turbulent kinetic energy and (b) temperature variance for the same filter lengths of the corresponding main plots.

This range of values has been chosen in order to analyse the behaviour of the resolved and subgrid velocity and temperature fields when the filter length is larger and smaller than the crossover scales  $\ell_{c,min}^{u*}$  and  $\ell_{c,min}^{\theta*}$ , respectively. We report the results for only two filter lengths, specifically  $\ell_F^* = 1$  and  $\ell_F^* = 3.1$  for the analysis of the velocity field and  $\ell_F^* = 0.7$  and  $\ell_F^* = 2.1$  for the analysis of the temperature field. In terms of relative dimensions, the smallest filter width is comparable with the thickness of the thermal boundary layer ( $\ell_F^* = 0.7$ ), whereas the largest one is slightly less than one fourth the height of the channel ( $\ell_F^* = 3.1$ ). Let us notice that the number of filter lengths that have been considered for this study is actually larger ( $\ell_F^* = \{0.7, 1, 1.4, 2.1, 3.1, 5.1\}$ ), but these results are not shown for the sake of conciseness. However, the main differences will be specifically stated when relevant.

#### 4.1. Analysis of the filtered single-point budgets

The main plots of figure 5(a,b) display the production of resolved turbulent kinetic energy,  $\bar{\pi}^u$ , and resolved temperature variance,  $\bar{\pi}^\theta$ , for two relevant filter lengths, together with their fully-resolved counterparts,  $\pi^u$  and  $\pi^\theta$ . It can be observed that the depletions of  $\bar{\pi}^u$  and  $\bar{\pi}^\theta$  with respect to the unfiltered terms can be considered negligible in case the filter width falls inside the homogeneous range, i.e.  $\ell_F^* < \ell_{c,min}^{u*} \approx 2.1$  and  $\ell_F^* < \ell_{c,min}^{\theta*} \approx 0.8$ , whereas they become important for large filter lengths. In particular, the difference between unfiltered and resolved productions is maximum in the near-wall region at  $z^* \approx 1$  and  $z^* \approx 0.5$ ; see figure 5(a) and 5(b) respectively. This behaviour is not surprising if we consider that the small scales that are filtered out produce mainly in the transitional layer rather than in other locations (see figure 3a-d); hence, the depletion that follows the filtering is expected to be more intense here than anywhere else.

The resolved dissipations  $\langle \bar{\epsilon} \rangle$  and  $\langle \bar{\chi} \rangle$  are affected by a stronger depletion as larger filter lengths are employed, as can be seen from the insets of figure 5(a,b). Inside the bulk region, the resolved dissipations are negligible with respect to the fully-resolved ones if the filter length is sufficiently larger than the minimum crossover scales, which means that the subgrid scales are the only ones interested by dissipative mechanisms away from the wall. On the other hand, the resolved scales start to make an important contribution to the dissipation inside the transitional and viscous layers, indeed the ratios  $\langle \bar{\epsilon} \rangle / \langle \epsilon \rangle$  and  $\langle \bar{\chi} \rangle / \langle \chi \rangle$  have been found to increase monotonically as the wall is approached.

The different contributions to the overall transport of  $\langle \bar{k} \rangle$  and  $\langle \bar{\theta}^2 \rangle$ , namely the

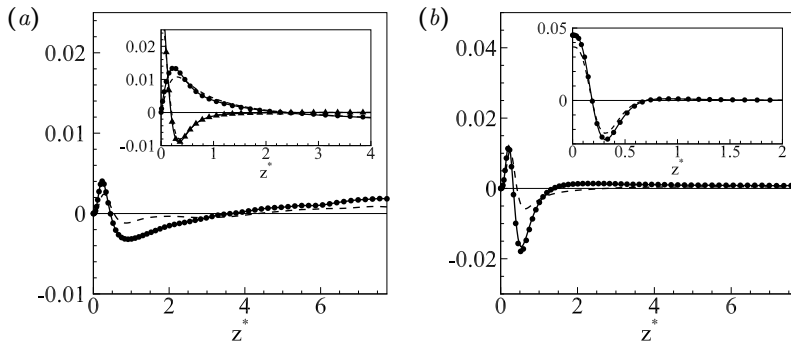


FIGURE 6. Unfiltered and resolved inertial transport of (a) turbulent kinetic energy (circles for the unfiltered case, solid line for  $\ell_F^* = 1.0$  and dashed line for  $\ell_F^* = 3.1$ ) and (b) temperature variance (circles for the unfiltered case, solid line for  $\ell_F^* = 0.7$  and dashed line for  $\ell_F^* = 2.1$ ). Insets: unfiltered and resolved (a) viscous and pressure transports of turbulent kinetic energy and (b) viscous transport of temperature variance for the same filter lengths.

inertial, pressure and viscous transports of resolved turbulent kinetic energy and the inertial and viscous transports of resolved temperature variance, are represented in figure 6(a,b). As well as the resolved productions, the resolved transports overlap the unfiltered counterparts when  $\ell_F^* < \ell_{c,min}^*$  and  $\ell_F^* < \ell_{c,min}^{u*}$  in accordance with the definition of the crossover scales  $\ell_c^*$  and  $\ell_c^{u*}$ . The component which seems to be more affected by the increase of the filter length is the inertial transport, whereas viscous and pressure contributions barely deplete with respect to the unfiltered references. The inertial transports are negative inside the transitional layer, meaning that turbulent velocity and temperature fluctuations are carried away by inviscid mechanisms and swept towards the wall and towards the core.

The rates at which energy and temperature variance are extracted by inertial mechanisms inside the transitional layer are particularly affected by depletions. This behaviour could be reasonably explained in terms of the coherent structures that populate turbulent convection, i.e. the so-called thermal plumes. See Togni *et al.* (2015) for a detailed analysis of thermal plumes conducted using the same DNS data set of the present work. These structures, which have a diameter comparable with the thermal boundary layer thickness ( $\delta_p^* \approx 0.5$ ), eject from the near-wall region and contribute significantly to the advective transport of turbulent kinetic energy and temperature variance towards the bulk. Hence, by filtering out the scales smaller than  $\ell_F^* = 2.1$  or  $\ell_F^* = 3.1$ , we lose trace of the coherent modes of convection and a depletion of the inertial transport is somehow expected.

Let us now consider the average subgrid dissipation  $\langle \epsilon_{sgs} \rangle$  and  $\langle \chi_{sgs} \rangle$ , represented as a function of  $z^*$  in the main plot of figure 7(a) and 7(b) respectively. Both terms are non-negative at every wall-distance and for both large and small filter lengths, meaning that subgrid scales behave, on average, as sinks of turbulent kinetic energy and temperature variance. The shape of the profiles changes quite evidently passing from small to large filter lengths and this alteration is marked for  $\langle \chi_{sgs} \rangle$ , where a local minimum appears around  $z^* = 0.5$ . The only *a priori* calculation of subgrid dissipation in RBC known to the authors is the one by Kimmel & Domaradzki (2000) for  $Ra = 6.3 \times 10^5$  and it shows a reasonable agreement with the preset results.

The subgrid transports  $t_{c,sgs}^u$  and  $t_{c,sgs}^\theta$  can be considered negligible for  $\ell_F^* < \ell_{c,min}^{u*}$  and  $\ell_F^* < \ell_{c,min}^*$ , whereas they become relevant at large filter widths. In the latter case, the subgrid transports and the corresponding inertial transports have similar profiles, i.e. the subgrid scales, apart from extracting a net amount of turbulent kinetic energy and



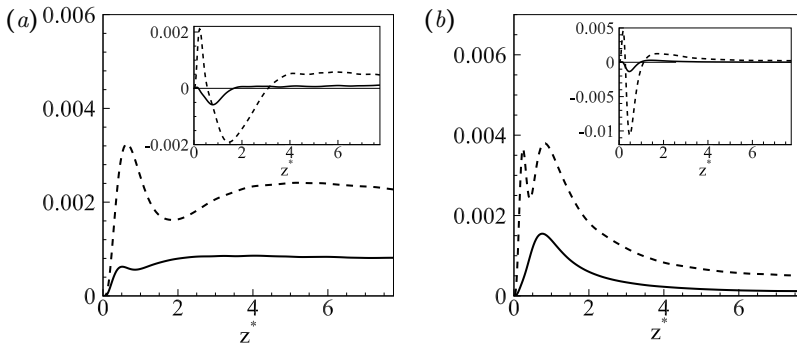


FIGURE 7. Profiles of subgrid dissipations (a)  $\langle \epsilon_{sgs} \rangle$  and (b)  $\langle \chi_{sgs} \rangle$  as a function of  $z^*$ , for  $\ell_F^* = 1.0$  (solid line) and  $\ell_F^* = 3.1$  (dashed line). Inset: profiles of SGS transport (a)  $t_{c,sgs}^u$  and (b)  $t_{c,sgs}^\theta$  as a function of  $z^*$ , for  $\ell_F^* = 0.7$  (solid line) and  $\ell_F^* = 2.1$  (dashed line).

temperature variance from the resolved ones ( $-\langle \epsilon_{sgs} \rangle < 0$  and  $-\langle \chi_{sgs} \rangle < 0$ ), transport resolved fluctuations from the transitional layer towards the bulk and the near-wall region. It can be seen by comparing the main plots in figure 6(a,b) with the insets in 7(a,b) that the resolved inertial transport and the subgrid redistribution terms are fairly comparable in magnitude inside the transitional layer, meaning that the nonlinear interactions between the resolved and the subgrid scales are as much important as the ones between resolved scales. In terms of flow topology, this could be related to the non-linear interactions between a hierarchy of structures living at subgrid level, namely the thermal plumes, and the large-scale circulation belonging to the resolved motion.

In closing this section, let us remark the role of the position of the filter length with respect to the characteristic scales  $\ell_c^{u*}$  and  $\ell_c^{\theta*}$ . Accordingly with their definition, the crossover scales  $\ell_c^{u*}$  and  $\ell_c^{\theta*}$  split the spectrum of convective turbulence in a range of large scales where the anisotropic production and inhomogeneous transport phenomena prevail and a range of small scales where turbulent cascade and dissipation processes dominate. This picture is also confirmed by considering low-pass filtered velocity and temperature fields, since, as shown by the filtered single-point budgets analysed so far, the production and transports of turbulent kinetic energy and temperature variance are correctly reproduced by the filtered fields when  $\ell_F^* < \ell_{c,min}^{u*}$  and  $\ell_F^* < \ell_{c,min}^{\theta*}$ . See Appendix A for further details on the transition from a well to a poorly resolved physics.

#### 4.2. Analysis of the filtered reduced Kolmogorov equation

In this section we analyze the filtered reduced Kolmogorov equation (2.11) at two distinct locations in physical space as representative of the scale-by-scale dynamics inside the bulk region and inside the transitional layer, and for two relevant filter lengths,  $\ell_F^* = 1.0$  and  $\ell_F^* = 3.1$ , which are respectively smaller and larger than the minimum crossover scale identified for the velocity field,  $\ell_{c,min}^{u*} \approx 2.1$ ; see figure 4(a). The terms of the filtered budget are reported for  $r_\rho^* \geq \ell_F^*$  to highlight that the range of scales for  $r_\rho^* < \ell_F^*$  actually belongs to the subgrid motion. Indeed, for  $r_\rho^* < \ell_F^*$ , the terms of the filtered budget are still formally defined but, numerically, the only collocation point defined by the filtered resolution is located at the trivial separation,  $r_\rho^* = 0$ .

Figure 8(a,b) shows the budget in the bulk,  $z^* = 3$ , and in the transitional layer,  $z^* = 0.7$ , for the smallest filter length considered,  $\ell_F^* = 1.0$ . It can be seen that both production and transport mechanisms are very well captured by the filtered fields, as the resolved terms  $\bar{\Pi}^u$  and  $\bar{T}_c^u$  fairly overlap the unfiltered counterparts,  $\Pi^u$  and  $T_c^u$ . This qualitative behaviour has been observed at every wall-distance and agrees with

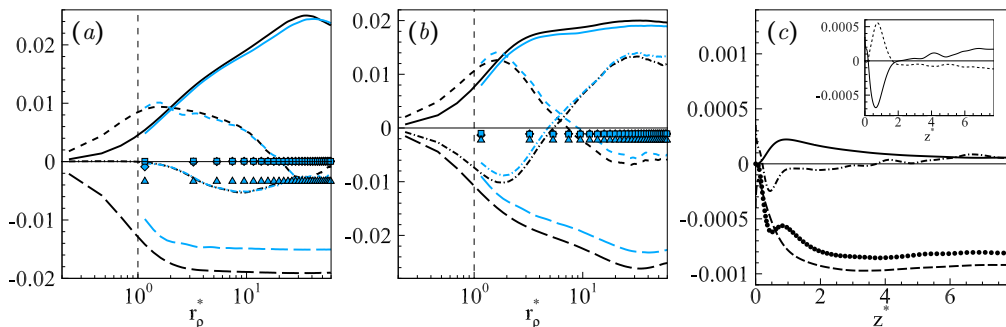
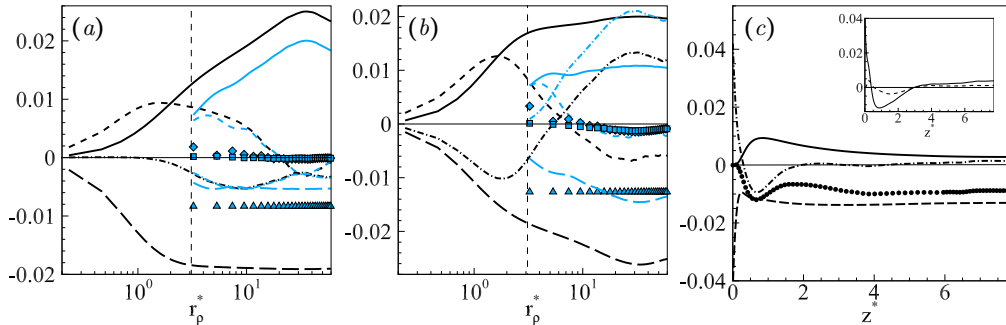


FIGURE 8. Scale-by-scale budgets (2.7) and (2.11) at (a)  $z^* = 3$  and (b)  $z^* = 0.7$  for  $\ell_F^* = 1.0$ . The unfiltered quantities are colored with black, the others are colored with blue (grey). Production (solid line), overall transport in physical space (dashed-dot line), transfer in the space of scales (dashed line), effective dissipation (long-dashed line),  $T_{c,sgs}^u$  (square),  $T_{r,sgs}^u$  (diamond),  $E_{sgs}^u$  (triangle). The vertical dashed lines denotes  $\ell_F^*$ . (c) Main plot: behaviour of  $-\langle \epsilon_{sgs} \rangle$  (circles),  $-\langle \epsilon' \rangle$  (long-dashed line),  $t_c^{u'} - t_{c,sgs}^u$  (dashed-dot line) and  $\pi^{u'}$  (solid line) as a function of  $z^*$  and for  $\ell_F^* = 1.0$ . Inset: profiles of  $t_c^{u'}$  (solid line) and  $-t_{c,sgs}^u$  (dashed line).

the choice of a filter length that is small enough to fall inside the homogeneous range, where the net source/drain of energy due to the inhomogeneous production and overall transport is weaker than the direct cascade towards dissipation. In these conditions, a single physical phenomenon is filtered out, namely the action of viscosity at the smallest scales; indeed, a clear depletion of the effective dissipation is observed,  $|\bar{E}_e^u| < |E_e^u|$ . Accordingly, the unique role of the subgrid scales is to drain resolved energy,  $E_{sgs}^u < 0$ , as much as the missed dissipation due to resolved motion, i.e. the sum of the resolved and subgrid dissipations recovers the unfiltered dissipation,  $\bar{E}_e^u + E_{sgs}^u \approx E_e^u$ . The transports of resolved energy in physical and scale space due to the action of subgrid scales are, on the contrary, negligible, as  $T_{c,sgs}^u \approx 0$  and  $T_{r,sgs}^u \approx 0$ .

For large filter lengths, we assist to a substantial change in the resolved dynamics. Figure 9(a) shows the scale-by-scale budget in the bulk of the flow at  $z^* = 3$  and for  $\ell_F^* = 3.1$ . Being  $\ell_F^* > \ell_{c,min}^{u*}$ , we expect a depletion of the effective amount of energy released at this wall-distance by the production and transport mechanisms, i.e.  $\bar{\Pi}^u + \bar{T}_c^u < \Pi^u + T_c^u$ , in accordance with the definition of the crossover scale  $\ell_{c,min}^{u*}$ . The inspection of figure 9(a) proves this expectation to be true and shows that the depletion is due only to the resolved production,  $\bar{\Pi}^u < \Pi^u$ , while  $\bar{T}_c^u \approx T_c^u$ . Also, the transport in the space of scales remains almost unaltered,  $\bar{T}_r^u \approx T_r^u$ , whereas, the effective dissipation is drastically reduced  $|\bar{E}_e^u| \ll |E_e^u|$ . Contrary to the previously shown cases where  $\ell_F^* < \ell_{c,min}^{u*}$ , now the effects of the SGS stresses on the resolved motion are not anymore due to viscous mechanisms. Indeed, the net energy exchange between resolved and subgrid scales,  $E_{sgs}^u$ , is not given alone by the dissipation occurring at subgrid level but also by a non-negligible production. This fact leads to a value of the subgrid dissipation that is the balance between these two concurrent mechanisms; hence, it does not allow to recover the unfiltered dissipation nor the unfiltered production. Indeed, we found that the subgrid scales drain energy from the resolved ones without recovering the actual value of dissipation, i.e.  $|\bar{E}_e^u + E_{sgs}^u| < |E_e^u|$ . Finally, the energy redistribution effect at resolved scales due to SGS stresses is found to be negligible in this region of the flow as  $T_{c,sgs}^u \approx 0$  and  $T_{r,sgs}^u \approx 0$ .

Closer to the wall, inside the transitional layer at  $z^* = 0.7$ , we still observe an erosion of the real physics; see figure 9(b). However, contrary to the bulk region, not only a depletion of the production mechanisms is observed here,  $\bar{\Pi}^u < \Pi^u$ , but also a modification of the

FIGURE 9. As figure 8 but for  $\ell_F^* = 3.1$ .

transports in physical and scale space becomes evident. In particular, we observe that the reverse energy transfer at large scales,  $I_r^u < 0$ , is not resolved being  $\bar{I}_r^u \approx 0$ , while the forward cascade at small scales,  $I_r^u > 0$ , is partially recovered. This aspect suggests that the reverse cascade is a nonlocal phenomenon (in scale space) involving a wide range of scales such that removing the eddies smaller than this filter length entails also a reduction of the transfer at large scales. The resulting depletion of the energy content of the large resolved scales is partially mitigated by an increase of the energy source due to the resolved spatial flux, since  $\bar{T}_c^u > T_c^u$ . Interestingly, the draining of the unfiltered spatial flux at small scales,  $T_c^u < 0$ , is not reproduced by the resolved motion. As shown in Togni *et al.* (2015), this double feature of the spatial flux is explained as a compound effect of spatial fluxes and reverse cascades. More explicitly, the presence of a reverse transfer in the space of scales deflects the spatial flux originating in the bulk so that in the transitional layer the large scales are gaining from the flux while small scales are still feeding the flux towards the wall. Since the reverse cascade occurring at large scale is not resolved for  $\ell_F^* > \ell_{c,min}^*$ , the deflection of the spatial flux does not take place and, as a consequence, all the resolved scales gain energy from the bulk of the flow,  $\bar{T}_c^u > 0$ . A difference with respect the bulk region is that now the SGS stresses contribute actively to the redistribution of resolved energy both in the physical space and in the space of scales, since the terms  $T_{c,sgs}^u$  and  $T_{r,sgs}^u$  are different from zero; see figure 9(b). The subgrid dissipation is negative,  $E_{sgs}^u < 0$ , as in the bulk of the flow; however, here  $E_{sgs}^u$  seems to take into account solely the missed dissipation at small scales being  $\bar{E}_e^u + E_{sgs}^u \approx E_e^u$ .

To understand the mechanisms determining the observed behaviour of the subgrid dissipation,  $E_{sgs}^u = -4 \langle \epsilon_{sgs} \rangle$ , we analyse in details the equation for the subgrid turbulent kinetic energy  $\langle k' \rangle = 0.5 \langle u'_i u'_i \rangle$ , namely

$$t_c^{u'} + \pi^{u'} - \langle \tilde{\epsilon}' \rangle - t_{c,sgs}^u + \langle \epsilon_{sgs} \rangle = 0, \quad (4.1)$$

where the terms denoted with the prime symbol and the ones without it in equation (2.13) are identical except for the replacement of velocity, temperature and pressure fields with the subgrid counterparts. Since we consider a spectral cutoff filter,  $\langle \bar{k} \rangle + \langle k' \rangle = \langle k \rangle$  and the sum of the subgrid and the resolved budgets corresponds to the unfiltered one.

Figure 8(c) shows the different terms of the budget (4.1) as a function of the wall-distance and for  $\ell_F^* = 1.0$ . As it can be seen from the main plot, the subgrid dissipation of resolved energy  $\langle \epsilon_{sgs} \rangle$  is almost balanced by the viscous dissipation at subgrid level  $\langle \tilde{\epsilon}' \rangle$  at every  $z^*$ . Indeed, the terms  $t_c^{u'} - t_{c,sgs}^u$  and  $\pi^{u'}$ , which are respectively the global transport and production of subgrid turbulent kinetic energy, have a small magnitude with respect to  $\langle \tilde{\epsilon}' \rangle$ . These aspects support the previously mentioned single physical role of the subgrid stresses for  $\ell_F^* < \ell_{c,min}^*$ , consisting of a drain of resolved energy due to

viscous mechanisms. Although the sum  $t_c^{u'} - t_{c,sgs}^u$  is lower in magnitude with respect to  $\langle \epsilon' \rangle$ , the separated contribution of the two transports terms,  $t_c^{u'}$  and  $-t_{c,sgs}^u$ , shown in the inset of figure 8(c), while small throughout the bulk of the flow, become comparable or even larger than  $\langle \epsilon_{sgs} \rangle$  closer the wall.

For large filter lengths, the mechanisms driving the subgrid dissipation  $E_{sgs}^u$  become more complex, as shown by figure 9(c) for  $\ell_F^* = 3.1$ . In the bulk region, the resolved energy released to the subgrid motion,  $\langle \epsilon_{sgs} \rangle$ , is balanced by viscous dissipation occurring at subgrid level  $\langle \epsilon' \rangle$  minus the production of the unresolved scales  $\pi^{u'}$ , while  $t_c^{u'} \approx 0$  and  $t_{c,sgs}^u \approx 0$ . The simplified relation  $-\langle \epsilon_{sgs} \rangle \approx \pi^{u'} - \langle \epsilon' \rangle$  seems to be satisfied for  $2 < z^* < 5$ . Closer to the wall, for  $z^* < 2$ , the subgrid dissipation  $\langle \epsilon_{sgs} \rangle$  is still driven by the dissipation and the production of subgrid scales, however the global transport in physical space is increased in magnitude with respect to the deep bulk, it grows even more approaching the wall and eventually balances the subgrid production around  $z^* = 0.7$ , thus explaining why  $\bar{E}_e^u + E_{sgs}^u \approx E_e^u$  inside the transitional layer. It should be stressed that the subgrid dissipation  $E_{sgs}^u$  balances the residual dissipation  $E_e^u - \bar{E}_e^u$  only in this case for  $\ell_F^* > \ell_{c,min}^{u*}$ , and that  $E_{sgs}^u$  is generally modulated by the inhomogeneous mechanisms taking place at subgrid level, namely the production and the transport of subgrid kinetic energy.

#### 4.3. Analysis of the filtered reduced Yaglom equation

We proceed by analyzing the filtered reduced Yaglom equation (2.12) inside the bulk,  $z^* = 3$ , and inside the transitional layer,  $z^* = 0.4$ , for the filter lengths  $\ell_F^* = 0.7$  and  $\ell_F^* = 2.1$ , which are respectively smaller and larger than the smallest crossover scale  $\ell_{c,min}^{\theta*} \approx 0.8$ ; see figure 10(a,b) and 11(a,b). In case  $\ell_F^* < \ell_{c,min}^{\theta*}$ , the resolved physics is very rich. As shown in figure 10(a,b), the production and transport mechanisms are captured well,  $\bar{\Pi}^\theta \approx \Pi^\theta$ ,  $\bar{T}_c^\theta \approx T_c^\theta$ , and so is the transfer between scales,  $\bar{I}_r^\theta \approx I_r^\theta$ . The effect of the SGS heat flux is to drain temperature variance,  $E_{sgs}^\theta < 0$ , with negligible redistribution effects at resolved scales, since  $T_{c,sgs}^\theta \approx 0$  and  $T_{r,sgs}^\theta \approx 0$ . Analogously to the velocity field, the condition  $\ell_F^* < \ell_{c,min}^{\theta*}$  allows to resolve the main inhomogeneous processes while leaving to the subgrid scales the duty of accounting solely for the diffusive mechanisms. Indeed, the rate at which temperature variance is drained by subgrid scales balances the missed dissipation at resolved scales, i.e.  $\bar{E}_e^\theta + E_{sgs}^\theta \approx E_e^\theta$ .

The picture changes when large filter widths are considered, as the resolved physics is strongly affected by the filtering operation and a significant portion of the relevant inhomogeneous mechanisms is left to be taken into account by the SGS heat flux. Accordingly, the scale-by-scale analysis for  $\ell_F^* = 2.1$  reveals that  $\bar{\Pi}^\theta + \bar{T}_c^\theta < \Pi^\theta + T_c^\theta$  both in the bulk and in the transitional layer; see figure 11(a,b). In particular, the production is adequately resolved in the bulk, where  $\bar{\Pi}^\theta \approx \Pi^\theta$ , but not inside the transitional layer. The reason is given by the fact that in the bulk region the production processes are weak and involve large scales while in the transitional layer production is stronger and small scales are active in the relative mechanisms. Contrary to the production, the transport mechanisms are poorly resolved throughout the entire domain. Hence, the picture consists of resolved fields where the production of temperature variance in the transitional layer is deteriorated and, as a consequence, also the spatial flux that sustains the temperature fluctuations in the other regions of the flow is drastically reduced, i.e.  $|\bar{T}_c^\theta| \ll |T_c^\theta|$ . For the same reasons, also the resolved cascade mechanisms are strongly depleted,  $|\bar{I}_r^\theta| \ll |I_r^\theta|$ . As it can be expected, this reduction of the forward and reverse transfers in the bulk and transitional layer, respectively, is more pronounced at large resolved scales where the intensity of these two resolved cascade phenomena is found to be almost null.

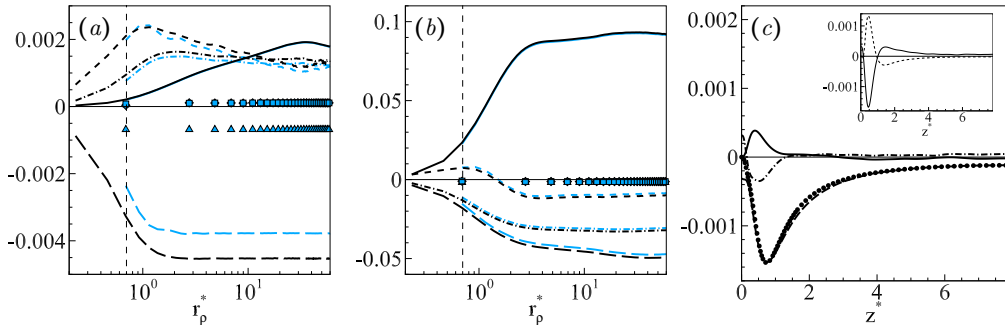


FIGURE 10. Scale-by-scale budgets (2.8) and (2.12) at (a)  $z^* = 3$  and (b)  $z^* = 0.4$  for  $\ell_F^* = 0.7$ . The unfiltered quantities are colored with black, the others are colored with blue (grey). Production (solid line), overall transport in physical space (dashed-dot line), transfer in the space of scales (dashed line), effective dissipation (long-dashed line),  $T_{c,sgs}^\theta$  (square),  $T_{r,sgs}^\theta$  (diamond),  $E_{sgs}^\theta$  (triangle). The vertical dashed lines denotes  $\ell_F^*$ . (c) Main plot: behaviour of  $-\langle\chi_{sgs}\rangle$  (circles),  $-\langle\chi'\rangle$  (long-dashed line),  $t_c^{\theta'} - t_{c,sgs}^\theta$  (dashed-dot line) and  $\pi^{\theta'}$  (solid line) as a function of  $z^*$  and for  $\ell_F^* = 0.7$ . Inset: profiles of  $t_c^{\theta'}$  (solid line) and  $-t_{c,sgs}^\theta$  (dashed line).

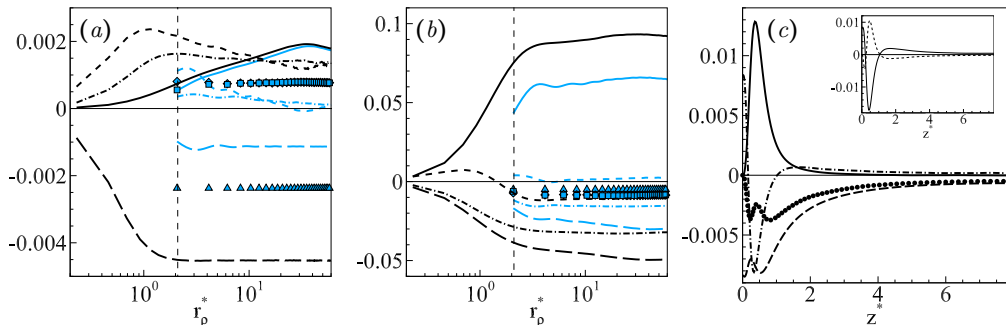
In agreement with these premises, the role of the SGS heat flux is relevant for the evolution of the resolved fields. In particular, the transport of resolved temperature variance both in physical and scale space is significantly determined by the interaction between resolved and unresolved scales, meaning that the subgrid redistributions  $T_{c,sgs}^\theta$  and  $T_{r,sgs}^\theta$  can not be neglected. The net temperature variance exchange between resolved and subgrid scales is negative both in the bulk and in the transitional layer,  $E_{sgs}^\theta < 0$ . However, this draining is not driven solely by diffusive mechanisms but also by inhomogeneous production and transport mechanisms which are significant at subgrid level for large filter lengths. As a consequence, the subgrid dissipation does not allow to recover the unfiltered rate of dissipation, i.e.  $|\bar{E}_e^\theta + E_{sgs}^\theta| < |E_e^\theta|$ .

In order to analyze more in details the mechanisms determining the behaviour of the subgrid dissipation,  $E_{sgs}^\theta = -2\langle\chi_{sgs}\rangle$ , we analyse in details the equation for the subgrid temperature variance  $\langle\theta'^2\rangle$ , namely

$$t_c^{\theta'} + \pi^{\theta'} - \langle\chi'\rangle - t_{c,sgs}^\theta + \langle\chi_{sgs}\rangle = 0, \quad (4.2)$$

where the terms denoted with the prime symbol and the ones without it in equation (2.14) are identical except for the replacement of velocity and temperature fields with the subgrid counterparts. Since we consider a spectral cutoff filter,  $\langle\bar{\theta}^2\rangle + \langle\theta'^2\rangle = \langle\theta^2\rangle$  and the sum of the subgrid and the resolved budgets corresponds to the unfiltered one.

Figure 10(c) and 11(c) show the budget (4.2) for  $\ell_F^* = 0.7$  and  $\ell_F^* = 2.1$ , respectively. In case of  $\ell_F^* < \ell_{c,min}^*$  (see figure 10c), it can be noticed that the subgrid dissipation is almost perfectly balanced by the viscous dissipation due to the subgrid scales,  $\langle\chi_{sgs}\rangle \approx \langle\chi'\rangle$ . The reason is that subgrid production, transport and the subgrid redistribution,  $\pi^{\theta'}$ ,  $t_c^{\theta'}$  and  $-t_{c,sgs}^\theta$ , are negligible inside the bulk of the flow. Closer to the wall, these terms become significant; however, they balance together and thus they do not contribute to the subgrid dissipation. These results suggest that, for  $\ell_F^* < \ell_{c,min}^*$ , the single relevant phenomenon that the SGS heat flux should take into account is the dissipation occurring at subgrid level. For this reason, as anticipated so far in the analysis of the scale-by-scale budgets, the combination of resolved and subgrid dissipation allows us to recover the unfiltered rate of dissipation, i.e.  $\bar{E}_e^\theta + E_{sgs}^\theta \approx E_e^\theta$ .

FIGURE 11. As figure 10 but for  $\ell_F^* = 2.1$ .

The picture becomes more complicated when large filter widths are considered. As it can be seen in figure 11(c), the subgrid dissipation  $\langle \chi_{sgs} \rangle$  is not only driven by  $\langle \chi' \rangle$  but it is influenced also by the subgrid production, transport and subgrid redistribution, in order  $\pi^{\theta'}$ ,  $t_c^{\theta'}$  and  $-t_{c,sgs}^{\theta}$ . In particular, in the bulk of the flow subgrid production is negligible and subgrid dissipation is driven by the balance between spatial transport and dissipation at subgrid scales,  $-\langle \chi_{sgs} \rangle \approx t_c^{\theta'} - t_{c,sgs}^{\theta} - \langle \chi' \rangle$ . Close to the wall, also the production at subgrid scales becomes very significant; hence, it does contribute to the value of subgrid dissipation. In conclusion, for large filter lengths, subgrid scales are involved in strong inhomogeneous processes, so that subgrid dissipation does not take into account solely the dissipation at subgrid scales but also production and transport mechanisms. As a result, the sum of resolved and subgrid dissipation does not allow to recover the unfiltered rate of dissipation, since  $|\bar{E}^{\theta} + E_{sgs}^{\theta}| < |E^{\theta}|$  as previously shown in the analysis of the filtered Yaglom equation.

The analysis of the filtered data set has important implications in LES. Classic eddy-viscosity/diffusivity models may provide a good estimation of the transfers between resolved and subgrid scales when  $\ell_F^* < \ell_{c,min}^{\theta}$ , as the main unresolved physics is the dissipation of turbulent kinetic energy and temperature variance. However, the inhomogeneous mechanisms become poorly resolved for larger filters and the SGS fields include highly dynamic eddies that contribute a significant portion of the production and transport besides dissipation, which may lead to modelling issues. Indeed, Smagorinsky-like models cannot account for the inhomogeneous mechanisms occurring at subgrid level, thus the exchanges between resolved and subgrid scales can hardly be copied.

Because the filtered Kolmogorov and the Yaglom equations have been proved to be of great support in describing the turbulent processes at different scales, locations in physical space and filter lengths, then we might consider the filtered scale-by-scale analysis as a valuable tool for testing the SGS models that are commonly employed in LES. This idea has been conceived by Cimarelli & De Angelis (2012) and brought to a novel assessment of the SGS stress model in turbulent channel flow (Cimarelli & De Angelis 2014). Future works will continue this line of research and consider the possibility to employ the filtered Kolmogorov and Yaglom equation to evaluate the performances of the state-of-the-art models employed for thermally driven turbulence.

## 5. Conclusions

Turbulence is commonly described as characterized by two different classes of processes: phenomena which occur in physical space, such as transport of momentum and energy, and phenomena which take place in the space of scales, such as the turbulent cascade.

The dual nature of these two processes and of the related theories is a spurious result of the observables used to study turbulence. In the present work, we develop and assess an alternative formalism to overcome this scale/position duality. The theoretical framework is based on the equations for the velocity and temperature structure functions, the so-called generalized Kolmogorov and Yaglom equations (Togni *et al.* 2015). Such a framework is here extended for the assessment of convective turbulence when a low-pass filtering operation is used. The use of Direct Numerical Simulation data of turbulent Rayleigh-Bénard convection at  $Ra = 1.0 \times 10^7$  and  $Pr = 0.7$  finally allows us to prove the reliability of the developed theoretical framework for the study of the resolved and subgrid dynamics in thermally driven turbulence by varying the filter length.

We first use the Kolmogorov and Yaglom equations to define two physically relevant characteristic scales for the velocity and temperature field. These scales,  $\ell_c^u$  and  $\ell_c^\theta$  respectively, decompose convective turbulence into a range of large scales where anisotropic production and inhomogeneous spatial transports prevail, and a range of small scales where, on the contrary, turbulent cascade and dissipation mechanisms dominate.

These crossover scales are then used for a rational assessment of the resolved and subgrid dynamics of convective turbulence as a function of the filter length employed. In this context, the most severe constraint is given by the characteristic scale imposed by the temperature field, rather than by the velocity field, as the kinematic crossover scale,  $\ell_c^u$ , exceeds the thermal crossover scale,  $\ell_c^\theta$ , at every wall-distance and, arguably, for every Prandtl larger than 0.7, as the smallest temperature scale decreases when  $Pr$  increases. The analysis of the generalized Kolmogorov and Yaglom equations extended to filtered convective turbulence single out that for filter lengths smaller than the crossover scales (i.e.  $\ell_F < \ell_{c,min}^\theta$ , as  $\ell_c^\theta < \ell_c^u$  everywhere), the resolved processes almost correspond to the exact ones except for a depletion of the resolved dissipations. In this case, the only role of the subgrid scales is to drain the amounts of energy and temperature variance that are not dissipated by resolved motion and temperature, that is to say,  $E_{sgs}^u \approx E_e^u - \bar{E}_e^u$  and  $E_{sgs}^\theta \approx E_e^\theta - \bar{E}_e^\theta$ . On the other hand, when  $\ell_F$  is sufficiently larger than  $\ell_{c,min}^\theta$ , a substantial fraction of the inhomogeneous range belongs to the subgrid scales; therefore, the physics of the flow is poorly resolved and the role of the subgrid scales is not only dissipative. With reference to the second issue, the exchanges of energy and temperature variance between resolved and subgrid scales,  $E_{sgs}^u$  and  $E_{sgs}^\theta$ , are set by the unresolved dissipations plus the inhomogeneous processes occurring at subgrid level; hence, the recovery of the unfiltered dissipation, namely  $E_e^u \approx \bar{E}_e^u + E_{sgs}^u$  and  $E_e^\theta \approx \bar{E}_e^\theta + E_{sgs}^\theta$ , does not occur in general.

Interestingly, the constraint given by the thermal crossover scale nondimensionalized with respect to twice the thermal boundary layer thickness,  $\ell_{c,min}^{\theta*} = \ell_{c,min}^\theta Nu/H = 0.8$ , is found to be substantially independent from the Rayleigh number, at least for the range of  $Ra$  considered in the present work. If confirmed, the developed criterion for the filter length would apply also for different Rayleigh numbers and fixed Prandtl as long as an estimation of the Nusselt number is available.

As a final remark, let us point out that in the LES framework, the classic eddy-viscosity/diffusivity models should be capable to reproduce the subgrid dynamics for  $\ell_F \approx \ell_{c,min}^\theta$ , as the only physics that needs to be copied is the dissipation of turbulent fluctuations occurring at subgrid level. On the other hand, the classic SGS models arguably suffer some deficiencies close to the walls and for  $\ell_F$  sufficiently larger than  $\ell_{c,min}^\theta$ , since they do not consider the mechanisms induced by spatial inhomogeneity, namely the subgrid production and transport in physical space. A future work will address both the *a priori* and *a posteriori* test of classic SGS models in order to better

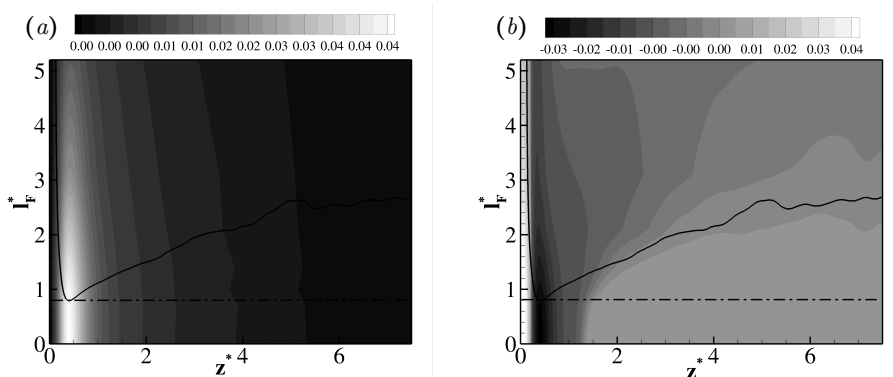


FIGURE 12. Intensities of the resolved temperature field processes as a function of the filter length and for different wall-distances. (a) Production of temperature variance  $\bar{\pi}^\theta(z^*, \ell_F^*)$ . For  $0 < \bar{\pi}^\theta(z^*, \ell_F^*) < 0.0025$  not equally spaced iso-contours are used to address the behaviour of production also in the bulk of the flow. (b) Overall inhomogeneous transport  $\bar{t}_c^\theta(z^*, \ell_F^*)$ . For  $-0.0025 < \bar{t}_c^\theta(z^*, \ell_F^*) < 0.0025$  not equally spaced iso-contours are used to address the behaviour of transport also in the bulk of the flow. The solid line reports the behaviour of the cross-over scale  $\ell_c^{\theta*}(z^*)$  while the dashed-dotted line the value of  $\ell_{c,min}^{\theta*} = 0.8$ .

assess the role of the filter length with respect to the crossover scales of RBC and, eventually, to formulate a physics-based SGS model that is capable to account also for the inhomogeneous processes occurring at subgrid scales when large filter lengths are employed.

## Appendix A. On the behaviour of the resolved energetics

Beside providing an exact theoretical framework for the study of the unfiltered, filtered and subgrid temperature and velocity fields both at the single-point and at the two-point level, the main body of the work makes use of the cross-over scales  $\ell_c^u$  and  $\ell_c^\theta$  to assess the behaviour of the large scale resolved fields as a function of the filter length  $\ell_F$  employed. In particular, it is shown that for  $\ell_F < \ell_{c,min}^\theta$ , both the large scale velocity and temperature fields essentially reproduce the unfiltered behaviours with exception of a fraction of viscous dissipation, which might be easily reproduced by classical subgrid scale closures. It is then shown that for large filter lengths compared to the cross-over scale, of the order of  $\ell_F \approx 3\ell_{c,min}^\theta$ , the resolved physics is poor and subgrid scale effects are more complex than a simple drain of kinetic energy and temperature variance, and thus challenging for turbulence closures. Hence, in the range  $\ell_{c,min}^\theta < \ell_F < 3\ell_{c,min}^\theta$  the resolved field experiences a transition from a well to a poor resolved physics. In this appendix, we provide additional details by addressing how this degradation of the resolved temperature and velocity fields occurs. To this purpose, we consider the behaviour of the production and spatial transport of turbulent kinetic energy and temperature variance as a function of the filter length employed,  $\ell_F^* = \{0.7, 1, 1.4, 2.1, 3.1, 5.1\}$ .

In figure 12(a), the behaviour of the production term of temperature variance is shown as a function of the filter length and for different wall-distances,  $\bar{\pi}^\theta = \bar{\pi}^\theta(z^*, \ell_F^*)$ . The most evident depletion of resolved production occurs in the near-wall region, where most of the temperature variance is produced, while in the bulk region the iso-contours are almost aligned in the vertical direction, thus denoting a weaker deterioration of production by increasing the filter length. This behaviour is reproduced by the cross-over scale  $\ell_c^{\theta*}(z^*)$ . In particular, its minimum in the transitional layer,  $\ell_{c,min}^{\theta*} = 0.8$ , is



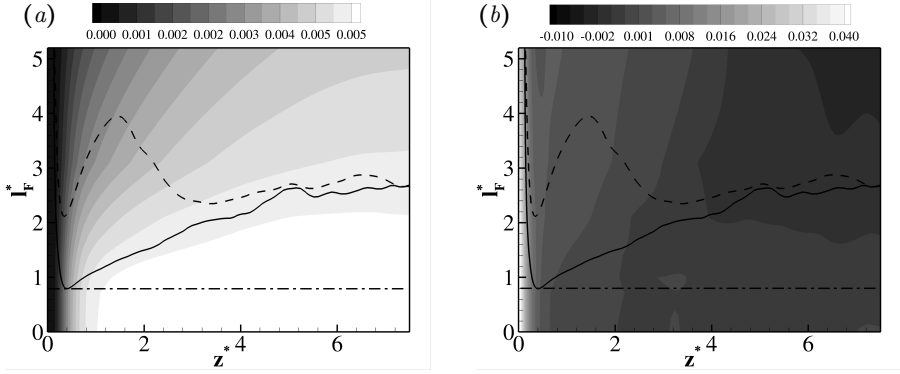


FIGURE 13. Intensities of the resolved velocity field processes as function of the filter length and for different wall-distances. (a) Production of turbulent kinetic energy  $\bar{\pi}^u(z^*, \ell_F^*)$ . (b) Overall inhomogeneous transport  $\bar{t}_c^u(z^*, \ell_F^*)$ . For  $-0.007 < \bar{t}_c^\theta(z^*, \ell_F^*) < -0.002$  not equally spaced iso-contours are used to address the behaviour of transport also in the bulk of the flow. The dashed line reports the behaviour of the cross-over scale  $\ell_c^{u*}(z^*)$  while the solid line denotes  $\ell_c^{\theta*}(z^*)$  as a reference. Also the value of  $\ell_{c,min}^{\theta*} = 0.8$  is reported with dashed-dotted line.

found to nicely capture the largest filter length that can be adopted before the appearance of a deterioration of the resolved production. The same observations can be drawn by analysing the behaviour of the overall spatial transport  $\bar{t}_c^\theta(z^*, \ell_F^*)$  shown in figure 12(b). Indeed, the peak of sink of temperature variance in the transitional layer which feeds the spatial transport towards the wall and bulk regions, is found to be significantly affected by the filter length. Again, this behaviour is nicely reproduced by the cross-over scale  $\ell_c^\theta$  which is found to capture with its minimum,  $\ell_{c,min}^{\theta*} = 0.8$ , the maximum value of the filter length before the appearance of a deterioration of the negative peak of the spatial transport in the transitional layer. Contrary to the production term, the spatial transport shows a non negligible filter length dependence also in the bulk of the flow. As highlighted by the iso-contours, this dependence is such that the depletion of the spatial transport occurs at increasingly large filter lengths by increasing the distance from the wall. Also in this case, the cross-over scale  $\ell_c^\theta$  is found to nicely reproduce such behaviour.

Let us now consider the behaviour of the resolved turbulent kinetic energy. In figure 13(a), the behaviour of the resolved production of turbulent kinetic energy is shown again as a function of the wall-distance and for different filter lengths,  $\bar{\pi}^u = \bar{\pi}^u(z^*, \ell_F^*)$ . Contrary to the temperature field, the production of turbulent kinetic energy is active in the bulk of the flow. This is the region where the effect of filtering is large while in the transitional and viscous layers is very weak as highlighted by the progressive vertical alignment of the iso-contours by decreasing the wall-distance. In the bulk of the flow, the effect of filtering shows a dependence on the wall-distance. In particular, the depletion of production occurs at increasingly large filter lengths by increasing the wall-distance. Such a behaviour is nicely captured by the cross-over scale  $\ell_c^{u*}(z^*)$ . Contrary to the bulk region, the transitional and viscous layers are dominated by the spatial transport  $\bar{t}_c^\theta(z^*, \ell_F^*)$  as shown in figure 13(b). In particular, the maximum of the transport occurs in the viscous layer and the effect of filtering is not particularly significant as shown by the almost vertical alignment of the iso-levels. The behaviour of the cross-over scale  $\ell_c^{u*}(z^*)$  is found to correctly reproduce such a small dependence. Interestingly, the cross-over scale shows also a transition from the transport dominated regions in the viscous and transitional layers to the production dominated region in the bulk of the flow. This

transition takes the form of a local maximum, thus denoting that the net compound role of production and transport in such a region involves larger scales.

In a LES context, the present results can be rationalized by using the behaviour of the cross-over scales. In particular, the temperature cross-over scale  $\ell_c^\theta$ , being always smaller than that for the velocity field,  $\ell_c^\theta < \ell_c^u$ , is recognized to nicely mark the transition from well to poorly resolved temperature and velocity fields as shown in figures 12 and 13. Furthermore, by considering the fact that the Rayleigh-Bénard problem is commonly solved by means of structured grids which are Cartesian in the wall-parallel planes (i.e., having constant spacing), the constraint given by  $\ell_{c,min}^{\theta*}$ , i.e.  $\ell_F^* \leq \ell_{c,min}^{\theta*} = 0.8$ , is recognized to identify a rule for the largest filter length which allows to recover the unfiltered production and transport processes in the entire flow domain, see the horizontal dashed-dotted line in figures 12 and 13. Let us finally remark that such a constraint is given nondimensionalized with respect to twice the thermal boundary layer thickness,  $\ell_{c,min}^{\theta*} = \ell_{c,min}^\theta Nu/H = 0.8$ , and, as shown in section §3 is found to be substantially independent on the Rayleigh number, at least for the range of  $Ra$  considered in the present work.

## REFERENCES

- AHLERS, G., BODENSCHATZ, E., FUNFSCHILLING, D., GROSSMANN, S., HE, X., LOHSE, D., STEVENS, R.J.A.M. & VERZICCO, R. 2012 Logarithmic temperature profiles in turbulent rayleigh-bénard convection. *Phys. Rev. Lett.* **109** (11), 114501.
- ANTONIA, R.A. & ORLANDI, P. 2003 Effect of schmidt number on small-scale passive scalar turbulence. *Appl. Mech. Rev.* **56** (6), 615–632.
- BRYAN, G. H., WYNGAARD, J. C. & FRITSCH, J. M. 2003 Resolution requirements for the simulation of deep moist convection. *Mon. Wea. Rev.* **131** (10), 2394–2416.
- BURATTINI, P., ANTONIA, R. A. & DANAILA, L. 2005 Scale-by-scale energy budget on the axis of a turbulent round jet. *J. Turbul.* (6), N19.
- CABOT, W. H. 1993 Large eddy simulations of time-dependent and buoyancy-driven channel flows. *Annual Research Briefs 1992* pp. 45–60.
- CHILLÀ, F. & SCHUMACHER, J. 2012 New perspectives in turbulent Rayleigh-Bénard convection. *Eur. Phys. J. E* **35** (7), 1–25.
- CIMARELLI, A. & DE ANGELIS, E. 2011 Analysis of the Kolmogorov equation for filtered wall-turbulent flows. *J. Fluid Mech.* **676**, 376–395.
- CIMARELLI, A. & DE ANGELIS, E. 2012 Anisotropic dynamics and sub-grid energy transfer in wall-turbulence. *Physics of Fluids (1994-present)* **24** (1), 015102.
- CIMARELLI, A. & DE ANGELIS, E. 2014 The physics of energy transfer toward improved subgrid-scale models. *Physics of Fluids (1994-present)* **26** (5), 055103.
- CIMARELLI, A., DE ANGELIS, E. & CASCIOLA, C. M. 2013 Paths of energy in turbulent channel flows. *J. Fluid Mech.* **715**, 436–451.
- CIMARELLI, A., DE ANGELIS, E., JIMÉNEZ, J. & CASCIOLA, C. M. 2016 Cascades and wall-normal fluxes in turbulent channel flows. *Journal of Fluid Mechanics* **796**, 417–436.
- CORRSIN, S. 1951 On the spectrum of isotropic temperature fluctuations in an isotropic turbulence. *J. Appl. Phys.* **22** (4), 469–473.
- DABBAGH, F., TRIAS, F.X., GOROBETS, A. & OLIVA, A. 2017 A priori study of subgrid-scale features in turbulent rayleigh-bénard convection. *Phys. Fluids* **29** (10), 105103.
- DABBAGH, F., TRIAS, F. X., GOROBETS, A. & OLIVA, A. 2016 New subgrid-scale models for large-eddy simulation of Rayleigh-Bénard convection. *J. Phys. Conf. Ser.* **745** (3), 032041.
- DANAILA, L., ANSELMET, F., ZHOU, T. & ANTONIA, R. A. 2001 Turbulent energy scale budget equations in a fully developed channel flow. *J. Fluid Mech.* **430**, 87–109.
- DANAILA, L., KRAWCZYNSKI, J.F., THIESSET, F. & RENOU, B. 2012 Yaglom-like equation in axisymmetric anisotropic turbulence. *Physica D: Nonlinear Phenomena* **241** (3), 216–223.
- DAVIDSON, P. A., PEARSON, B. R. & STAPLEHURST, P. 2004 How to describe turbulent energy

- distributions without the fourier transform. In *Proceedings of the AFMC 15*. University of Sydney.
- DEARDORFF, J. W. 1974 Three-dimensional numerical study of the height and mean structure of a heated planetary boundary layer. *Bound.-Layer Meteor.* **7** (1), 81–106.
- DOMARADZKI, J. A., LIU, W., HÄRTEL, C. & KLEISER, L. 1994 Energy transfer in numerically simulated wall-bounded turbulent flows. *Phys. Fluids* **6**, 1583–1599.
- DUPUY, D., TOUTANT, A. & BATAILLE, F. 2018 Turbulence kinetic energy exchanges in flows with highly variable fluid properties. *J. Fluid Mech.* **834**, 5–54.
- GAUDING, M., WICK, A., PITSCHE, H. & PETERS, N. 2014 Generalised scale-by-scale energy-budget equations and large-eddy simulations of anisotropic scalar turbulence at various schmidt numbers. *Journal of Turbulence* **15** (12), 857–882.
- GAYEN, B., HUGHES, G.O. & GRIFFITHS, R.W. 2013 Completing the mechanical energy pathways in turbulent rayleigh-benard convection. *Phys. Rev. Lett.* **111** (12), 124301.
- GROSSMANN, S. & LOHSE, D. 2000 Scaling in thermal convection: a unifying theory. *J. Fluid Mech.* **407**, 27–56.
- HÄRTEL, C., KLEISER, L., UNGER, F. & FRIEDRICH, R. 1994 Subgrid-scale energy transfer in the near-wall region of turbulent flows. *Phys. Fluids* **6** (9), 3130–3143.
- HILL, R. J. 2002 Exact second-order structure-function relationships. *J. Fluid Mech.* **468**, 317–326.
- KIMMEL, S. J. & DOMARADZKI, J. A. 2000 Large eddy simulations of Rayleigh–Bénard convection using subgrid scale estimation model. *Phys. Fluids* **12** (1), 169–184.
- KOLMOGOROV, A. N. 1941*a* Dissipation of energy in locally isotropic turbulence. *Dokl. Akad. SSSR* **32**, 16–18.
- KOLMOGOROV, A. N. 1941*b* The local structure of turbulence in incompressible viscous fluid for very large Reynolds numbers. In *Dokl. Akad. Nauk SSSR*, , vol. 30, pp. 301–305. JSTOR.
- LILLY, D. K. 1962 On the numerical simulation of buoyant convection. *Tellus* **14** (2), 148–172.
- LILLY, D. K. 1967 The representation of small scale turbulence in numerical simulation experiments .
- LIU, S., MENEVEAU, C. & KATZ, J. 1994 On the properties of similarity subgrid-scale models as deduced from measurements in a turbulent jet. *J. Fluid Mech.* **275**, 83–119.
- LOHSE, D. & XIA, K.-Q. 2010 Small-scale properties of turbulent Rayleigh–Bénard convection. *Annu. Rev. Fluid Mech.* **42**, 335–364.
- MARATI, N., CASCIOLA, C. M. & PIVA, R. 2004 Energy cascade and spatial fluxes in wall turbulence. *J. Fluid Mech.* **521**, 191–215.
- MASON, P. J. 1989 Large-eddy simulation of the convective atmospheric boundary layer. *J. Atmos. Sci.* **46** (11), 1492–1516.
- OBUKHOV, A. M. 1968 Structure of the temperature field in turbulent flow. *Tech. Rep.*. DTIC Document.
- PIOMELLI, U. 1999 Large-eddy simulation: achievements and challenges. *Prog. Aerosp. Sci.* **35** (4), 335–362.
- PIOMELLI, U. & BALARAS, E. 2002 Wall-layer models for large-eddy simulations. *Annu. Rev. Fluid Mech.* **34** (1), 349–374.
- PIOMELLI, U., CABOT, W. H., MOIN, P. & LEE, S. 1991 Subgrid-scale backscatter in turbulent and transitional flows. *Phys. Fluids A* **3** (7), 1766–1771.
- POPE, S. B. 2001 Turbulent flows.
- PORTÉ-AGEL, F., PARLANGE, M. B., MENEVEAU, C. & EICHINGER, W. E. 2001 A priori field study of the subgrid-scale heat fluxes and dissipation in the atmospheric surface layer. *J. Atmos. Sci.* **58** (18), 2673–2698.
- SERGEANT, A., JOUBERT, P. & LE QUÉRÉ, P. 2006 Large-eddy simulation of turbulent thermal convection using a mixed scale diffusivity model. *Prog. Comput. Fluid Dy.* **6** (1-3), 40–49.
- SIGGIA, E. D. 1994 High Rayleigh number convection. *Annu. Rev. Fluid Mech.* **26** (1), 137–168.
- SMAGORINSKY, J. 1963 General circulation experiments with the primitive equations. 1. The basic experiment. *Mon. Wea. Rev.* **91** (3), 99–164.
- TOGNI, R., CIMARELLI, A. & DE ANGELIS, E. 2015 Physical and scale-by-scale analysis of Rayleigh–Bénard convection. *J. Fluid Mech.* **782**, 380–404.
- VALENTE, P. C. & VASSILICOS, J. C. 2015 The energy cascade in grid-generated non-equilibrium decaying turbulence. *Phys. Fluids* **27** (4), 045103.

- VAN REEUWIJK, M., JONKER, H. J. J. & HANJALIĆ, K. 2005 Identification of the wind in Rayleigh-Bénard convection. *Phys. Fluids* **17** (5), 051704.
- YAGLOM, A. M. 1949 On the local structure of a temperature field in a turbulent flow. *Dokl. Akad. SSSR* **69**, 743.